Nanoscale cellular organization of viral RNA and proteins in SARS-CoV-2 replication organelles

Leonid Andronov*[1], Mengting Han*[2], Yanyu Zhu[2], Anish R. Roy[1], Andrew E. S. Barentine[1], Jaishree Garhyan[3], Lei S. Qi[2,4,5], W.E. Moerner[1,4]

[1]Department of Chemistry; [2]Department of Bioengineering; [3]In Vitro Biosafety Level 3 (BSL-3) Service Center, School of Medicine; [4]Sarafan ChEM-H; Stanford University, Stanford, CA 94305 U.S.A. [5]Chan Zuckerberg Biohub – San Francisco, San Francisco, CA 94158 U.S.A.

*These authors contributed equally.

#Correspondence to: W. E. Moerner, wmoerner@stanford.edu; Lei S. Qi, sqi@stanford.edu

Abstract:

The SARS-CoV-2 viral infection transforms host cells and produces special organelles in many ways, and we focus on the replication organelle where the replication of viral genomic RNA (vgRNA) occurs. To date, the precise cellular localization of key RNA molecules and replication intermediates has been elusive in electron microscopy studies. We use super-resolution fluorescence microscopy and specific labeling to reveal the nanoscopic organization of replication organelles that contain vgRNA clusters along with viral double-stranded RNA (dsRNA) clusters and the replication enzyme, encapsulated by membranes derived from the host endoplasmic reticulum (ER). We show that the replication organelles are organized differently at early and late stages of infection. Surprisingly, vgRNA accumulates into distinct globular clusters in the cytoplasmic perinuclear region, which grow and accommodate more vgRNA molecules as infection time increases. The localization of ER labels and nsp3 (a component of the double-membrane vesicle, DMV) at the periphery of the vgRNA clusters suggests that replication organelles are enclosed by DMVs at early infection stages which then merge into vesicle packets as infection progresses. Precise co-imaging of the nanoscale cellular organization of vgRNA, dsRNA, and viral proteins in replication organelles of SARS-CoV-2 may inform therapeutic approaches that target viral replication and associated processes.

Keywords: SARS-CoV-2 coronavirus, viral replication, fluorescence imaging, super-resolution fluorescence microscopy, viral RNA localization, COVID-19, viral proteins, cell infection

Introduction

Due to its global health impact, the SARS-CoV-2 coronavirus and its infection of mammalian cells have been the subject of a large number of studies across multiple fields. Biochemical methods have allowed researchers to investigate the interactions between the viral oligonucleotides and the host proteins *in vitro* and in cellular extracts, leading to much insight[1,2]. There have also been electron microscopy (EM) studies of resin-embedded samples as well as vitrified samples using cryo-electro tomography, all of which have been profiting from the large increase in EM resolution and contrast in recent years. These EM studies can provide very high-resolution structures of protein complexes as well as tomograms of organelles in the cellular context. High-contrast filamentous structures and membranes appear regularly in such images, allowing identification of single- and double-membrane vesicles (DMVs)[3-5]. However, the all-important viral RNA and associated proteins are challenging to identify by EM due to a lack of specific contrast. While some researchers have detected RNA-like filaments in vesicles[4,5], further investigations are needed to identify specific viral RNAs in the cellular context.

Fluorescence microscopy offers a highly useful and complementary set of capabilities, most importantly the specific labeling of proteins or RNA sequences. However, conventional diffraction-limited (DL) fluorescence microscopy, with its resolution constrained to ~250 nm, is unable to resolve the tiny structures that are hidden in a blurred DL image. Super-resolution (SR) microscopy based on single molecules (PALM[6], (d)STORM[7,8]) or on structured patterns of molecular depletion (STED[9], SIM[10]), however, offers far better optical resolution down to 10 nm and below. A wealth of important cellular patterns and structures have been identified in recent years, such as the banding patterns of axonal proteins in neuronal cells[11] and many others[12-14]. The specificity of SR imaging is useful to apply to the study of viral genomic RNA (vgRNA) and other RNA molecules as well as protein players involved in coronavirus infection of cells, demonstrated previously for the less pathogenic human coronavirus 229E (HCoV-229E)[15].

In this work, we apply multicolor confocal microscopy and SR microscopy to explore the localization patterns of viral RNA and protein molecules for SARS-CoV-2 during the early and late infection of mammalian cells. We focus particularly on viral genomic RNA (vgRNA) and its relative,

77 the double-stranded RNA (dsRNA) that forms between the (+) sense vgRNA and the (-) sense copy.
78 After the initial infection with a few copies of vgRNA, more vgRNA and dsRNA are synthesized by
79 the RNA-dependent RNA polymerase complex (RdRp), an early essential enzyme formed by
80 ribosomal polyprotein synthesis and the viral proteases. We also co-image a series of molecules,
81 including membrane markers, nucleocapsid protein, spike protein, and the nsp3 protein (reported
82 to be a major component of a molecular pore spanning both membranes of DMVs[16]), all to
83 provide context and support for the view that vgRNA, dsRNA, and RdRp act spatially in replication
84 organelles (ROs) during virus replication. Thus, we provide key information about where these
85 important players are found in infected cells and how they change with time during infection. Our
86 results yield a nanoscale optical readout of viral nucleic acid organization during SARS-CoV-2
87 infection, highlight the structural importance of ROs, and could potentially benefit development
88 of future therapeutic approaches.

89

90 **Results**

91 *Labeling and imaging of SARS-CoV-2 virions*

92 To specifically detect SARS-CoV-2 vgRNA, we applied RNA fluorescence *in situ* hybridization (RNA
93 FISH) with 48 antisense DNA oligonucleotide probes[17] specifically targeting the open reading
94 frame 1a (ORF1a) region which is only present in vgRNA and not in sgRNAs, insuring detection of
95 only full-length viral (+)vgRNA (Fig. 1a). Each probe was conjugated with a single blinking
96 fluorophore for (d)STORM (direct Stochastic Optical Reconstruction Microscopy)[8]. To test this
97 labelling and imaging approach, we first imaged vgRNA along with SARS-CoV-2 spike protein in
98 purified virions (Extended Data Fig. 1). While the size of SARS-CoV-2 virions is too small to resolve
99 in conventional DL fluorescence microscopy (Extended Data Fig. 1a), in SR the internal concentric
100 organization of the virions can be observed with vgRNA found in their center and spike at the
101 surface (Extended Data Fig. 1b). The labelling efficiency with these probes is around 6 dyes/vgRNA
102 in partially Proteinase K-digested virions, which was higher than in intact virions due to poorer
103 accessibility of their vgRNA (Extended Data Fig. 1c-i).

104 Next, we imaged SARS-CoV-2 infected Vero E6 cells that were fixed at 24 hours post infection (hpi)
105 and then labeled for immunofluorescence imaging (Methods). Spike and nucleocapsid SR
106 microscopy in these cells revealed assembled virions mostly at the cellular periphery, often at
107 cytoplasmic tubular projections, indicating active viral production (Extended Data Fig. 1j), similar
108 to previously reported results[5,18]. We now turn to the main focus of this study, the replication of
109 viral genomic RNA.

110

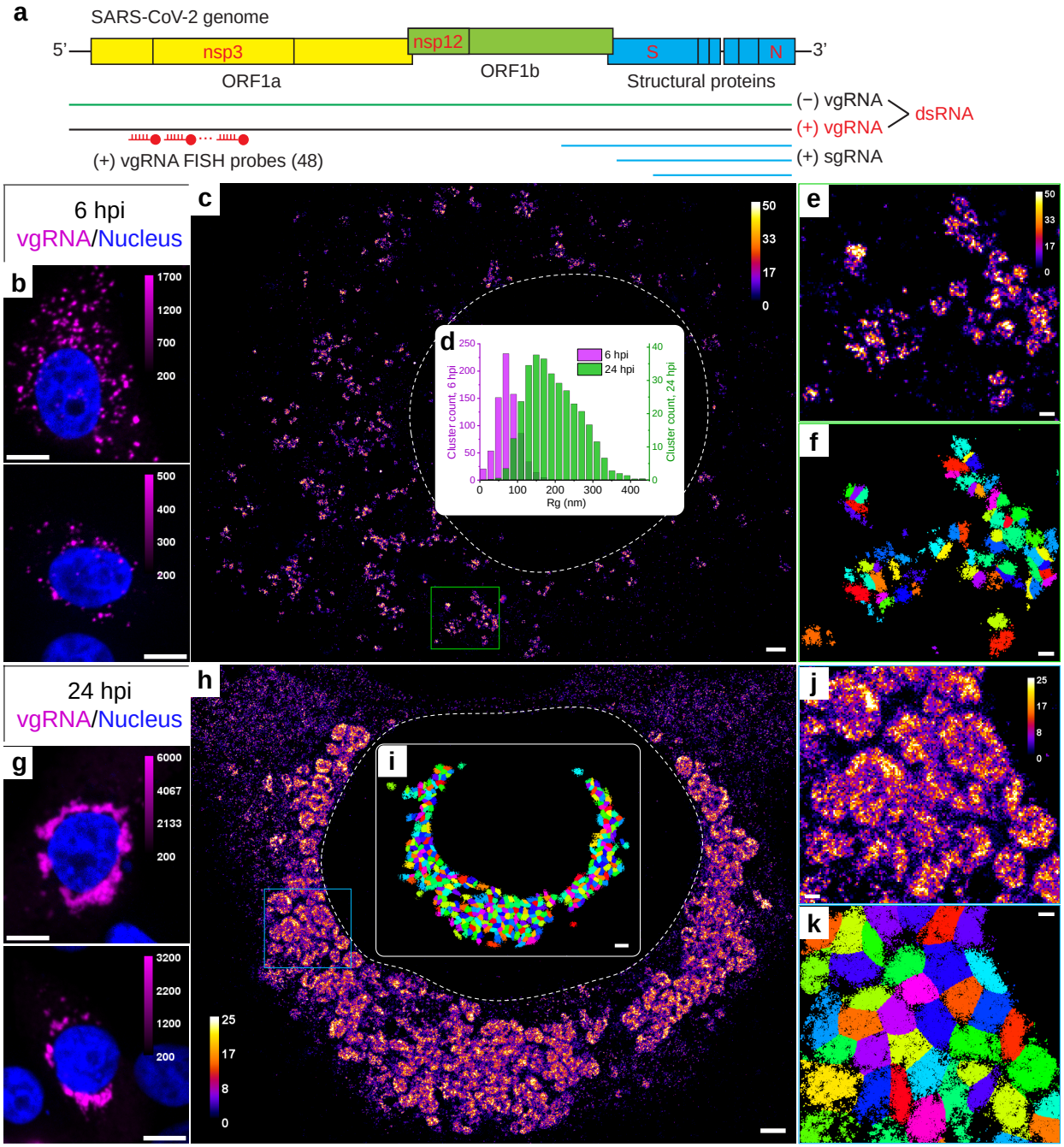

Fig. 1: Clustering of vgRNA in the cytoplasm of infected cells.

a, Scheme of SARS-CoV-2 genome with constructs used for its detection in infected cells. 48 antisense DNA oligonucleotide probes were used to target the ORF1a-coding region of vgRNA that is exclusive to the (+)vgRNA and does not occur in the sgRNAs. The RNA FISH probes are conjugated with AF647 or CF568. **b**, Representative confocal images of vgRNA in infected Vero E6 cells at 6 hpi display scattered DL puncta. **c**, Representative SR image of an infected cell at 6 hpi reveals distinct vgRNA clusters in the cytoplasm. **d**, Histogram of the radii of gyration (Rg) of the

vgRNA clusters indicate their size increase between 6 hpi (magenta) and 24 hpi (green). **e**, Zoomed-in region of the SR image (green frame in **c**) displays an agglomeration of vgRNA clusters. **f**, BIC-GMM cluster analysis of the region shown in **e**. **g**, Representative confocal images of vgRNA in infected Vero E6 cells at 24 hpi display large DL foci in the perinuclear region of the cytoplasm. **h**, Representative SR image of an infected cell at 24 hpi reveals large perinuclear vgRNA clusters. **i**, BIC-GMM cluster analysis of the cell shown in **h**. **j**, Zoomed-in region of the SR image (blue frame in **h**) displays dense vgRNA clusters. **k**, BIC-GMM cluster analysis of the region shown in **j**. Scale bars, 10 µm (**b**, **g**), 1 µm (**c**, **h**), 200 nm (**e**, **f**, **j**, **k**). Dashed lines in **c** and **h** indicate the position of the cell nucleus. Localizations that belong to the same cluster in **f**, **i**, **k** are depicted with the same color. Color bars in **c**, **e**, **h**, **j** show the number of SM localizations within each SR pixel (20 x 20 nm^2).

SARS-CoV-2 genomic RNA clusters in cytoplasm of infected cells

Confocal screening demonstrated three patterns of intracellular vgRNA localization (Extended Data Fig. 2a): scattered puncta in the cytoplasm (Type 1, Fig. 1b), appearance of bright foci in the perinuclear region (Type 2, Extended Data Fig. 2a), and concentration of vgRNA into large dense structures that occupy most of the perinuclear region (Type 3, Fig. 1g). We find that Type 1 cells were most abundant at 6 hpi, and Type 3 cells at 24 hpi, indicating that the vgRNA localization progresses from Type 1 to Type 3 as infection advances in time (Extended Data Fig. 2b). We also find that the cell-integrated vgRNA FISH signal in infected cells increases 2.2x on average from 6 to 24 hpi (Extended Data Fig. 2c), representing active viral replication and accumulation of vgRNA inside the cells.

The higher spatial resolution of SR microscopy revealed that at 6 hpi (Type 1 and Type 2 cells), most vgRNA localizes into clusters with an approximately round shape and a diameter of 100-250 nm that scatter in the cytoplasm (Fig. 1c, e). At 24 hpi (Type 2 and Type 3 cells), the vgRNA localization pattern transformed into a fascinating dense perinuclear network of approximately round, often hollow structures with a diameter of 300-700 nm (Fig. 1h, j). To quantify the transformation of vgRNA to clusters in infected cells, we performed a Bayesian Information Criterion-optimized Gaussian Mixture Model clustering analysis (BIC-GMM) (Fig. 1f, i, k; See

149 Methods). This analysis showed an increase in the median vgRNA cluster size (radius of gyration)
150 from 73 nm at 6 hpi to 187 nm at 24 hpi (Fig. 1d, see inset) reflecting the drastic change in vgRNA
151 localization pattern.

152 Besides dense vgRNA clusters, we observe isolated localizations of individual vgRNA molecules
153 scattered in the cytoplasm at both time points, in line with previously reported results on the
154 229E virus[15,17]. These appear as a haze in confocal images (Extended Data Fig. 2a, Type 3) but are
155 resolved as sparse nanoscale puncta (d < 50 nm) in SR (Fig. 1h, Extended Data Fig. 3a) which we
156 assume to be single vgRNA copies (even though the puncta are more dense at 24 hpi). Using the
157 average number of single-molecule (SM) localizations per vgRNA punctum as a calibration for the
158 number of localizations per single vgRNA, we estimated the average number of vgRNA molecules
159 in the vgRNA clusters to be around 26 vgRNA/cluster at 6 hpi, increasing by almost an order of
160 magnitude to 181 vgRNA/cluster at 24 hpi (Extended Data Fig. 3b-c).

161

162 *dsRNA associates with vgRNA clusters*

163 Next, we proceeded to assess the relation of vgRNA cluster locations to viral replication. For this,
164 we immunofluorescently labelled an intermediate of coronavirus replication and transcription,
165 the hybridized dsRNA objects composed of (+) sense vgRNA and (-) sense copy, and co-imaged
166 dsRNA with vgRNA using two-color confocal and SR microscopy. These targets appeared mostly
167 colocalized at both timepoints at low resolution (Fig. 2a-b), suggesting that vgRNA clusters are
168 often found close to the replication centers of SARS-CoV-2. SR microscopy revealed that dsRNA
169 aggregates into clusters of a relatively compact size (d ≈ 100-200 nm) with distinct patterns of
170 colocalization with vgRNA at 6 or 24 hpi (Fig. 2c-e).

171 To quantify the spatial relationship between dsRNA and vgRNA, we conducted pair-pair
172 correlation analysis[19]. We calculated a bivariate pair-correlation function $g_{12}(r)$, *i.e.*, the
173 distribution of the pairwise distances between the localizations of the two species[20]. The function
174 is computed only in perinuclear regions and is normalized in a way that $g_{12}(r) = 1$ for two randomly
175 and homogeneously distributed species, signifying complete spatial randomness (CSR). Closely
176 associated or colocalized species have a prevalence of short pairwise distances resulting in a peak

177 in $g_{12}(r)$ near $r = 0$, while anti-correlated species lack short interparticle distances, which lowers
178 $g_{12}(r)$ at $r = 0$ followed by peaking at $r > 0$.

179 At early infection stages (6 hpi), dsRNA clusters appear closely associated with or adjacent to
180 vgRNA clusters both visually and by pair-pair correlation analysis (Fig. 2c, f). By contrast, during
181 late infection (24 hpi), dsRNA clusters anticorrelate with vgRNA at short distance scales with an
182 average separation between them around 120 nm as indicated by bivariate pair-correlation
183 functions $g_{12}(r)$ (Fig. 2g). Moreover, at 24 hpi, dsRNA clusters can often be found in the voids of
184 the large vgRNA structures (Fig. 2d), suggesting their possible concentric localization in the same
185 ROs.

186 Contrary to vgRNA, the size of dsRNA clusters slightly decreases and the total brightness of
187 cellular dsRNA labelling does not significantly change between 6 hpi and 24 hpi (Fig. 2e, Extended
188 Data Fig. 2d). Interestingly, at 6 hpi but not at 24 hpi, the dsRNA signal per cell positively correlates
189 with that of vgRNA signal (Extended Data Fig. 2f-g). These findings indicate that the amount of
190 dsRNA increases at early infection but reaches saturation by 24 hpi. This may suggest that after
191 the rapid initial production of a dsRNA pool, further generation of (-) sense copies slows down
192 and the replication shifts to the generation of vgRNA from the pool of available (-) sense copy
193 templates, which is common in other coronaviruses[21]. Similar anticorrelation between the
194 localizations of vgRNA and dsRNA, but constant dsRNA cluster size with infection time have been
195 previously observed for the 229E coronavirus[15], consistent with the related biology of 229E and
196 SARS-CoV-2.

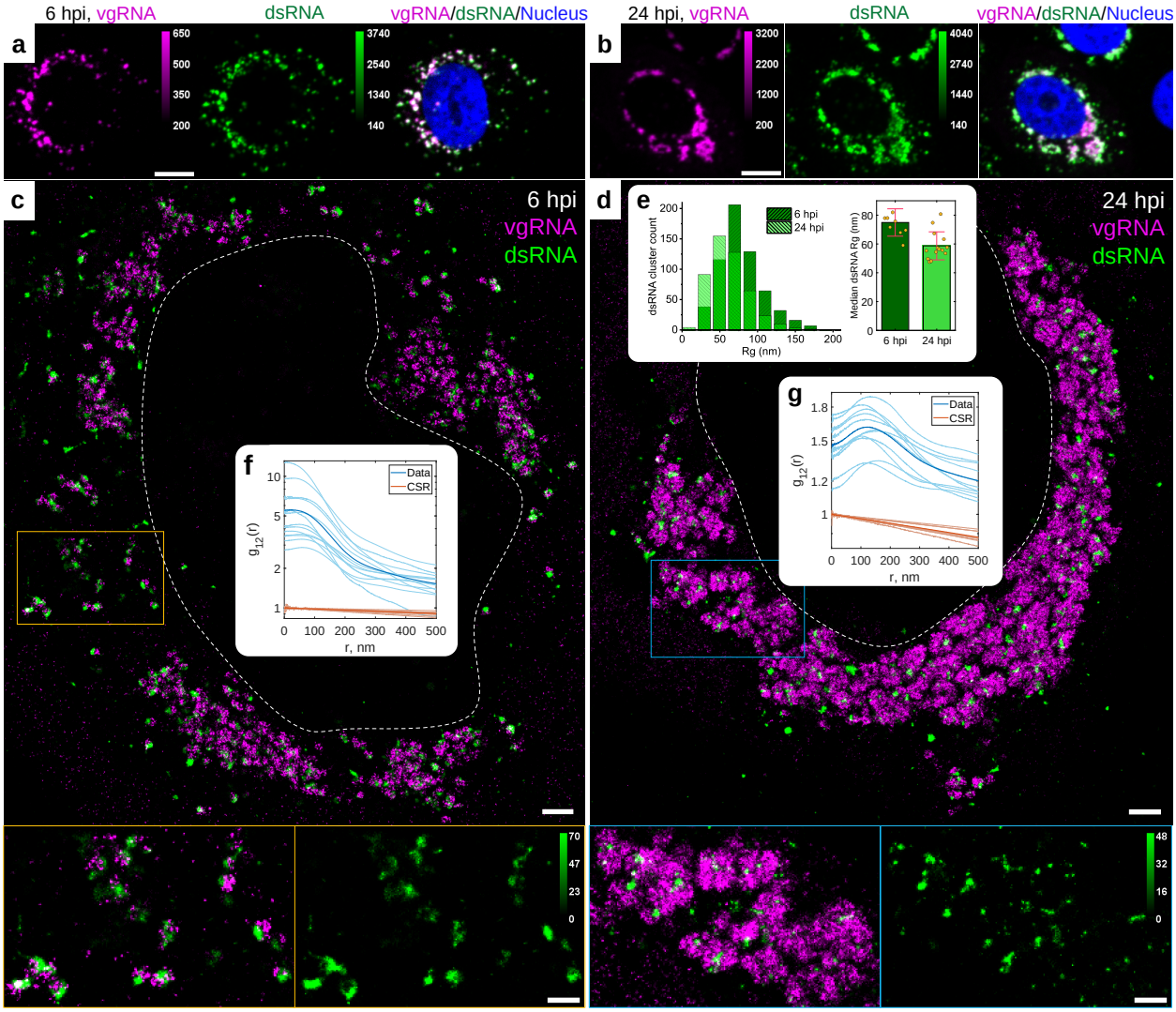

Fig. 2: Association of dsRNA with vgRNA clusters

a-**b**, Representative confocal images of SARS-CoV-2 infected cells display DL colocalization between dsRNA (green) and vgRNA (magenta) at both 6 hpi (**a**) and 24 hpi (**b**). **c**-**d**, Representative SR images of SARS-CoV-2 infected cells indicate association between dsRNA and vgRNA at 6 hpi (**c**) and short-range anti-correlation often with concentric localization at 24 hpi (**d**). Bottom panels, zoomed-in images of corresponding colored boxes. **e**, Histogram of Rg of dsRNA clusters as determined by the BIC-GMM cluster analysis (left). Median Rg of dsRNA clusters significantly decreases between 6 hpi and 24 hpi (right). p-value = $8 \cdot 10^{-4}$, two-tailed t-test. (**f**-**g**), Bivariate pair-correlation functions $g_{12}(r)$ calculated between the localizations of dsRNA and vgRNA indicate close association at 6 hpi (**f**) and nanoscale anti-correlation at 24 hpi (**g**). CSR, complete spatial randomness. Thin lines correspond to $g_{12}(r)$ of individual cells and bold lines are the mean values of $g_{12}(r)$ from all analyzed cells. Scale bars, 10 µm (**a**-**b**), 1 µm (**c**-**d**), 500 nm (**c**-**d**, bottom panels). Dashed lines in **c** and **d** indicate the position of the cell nucleus.

211 *vgRNA clusters denote the replication centers of SARS-CoV-2 genome*

212 To investigate SARS-CoV-2 replication activity at the vgRNA clusters in more detail, we co-imaged
213 them with the RdRp complex, the replicating SARS-CoV-2 RNA-dependent RNA polymerase[22,23],
214 using immunofluorescent labelling of its catalytic subunit nsp12[24]. In confocal images, nsp12
215 adopts a similar pattern as vgRNA, colocalizing with it at both 6 hpi and 24 hpi (Fig. 3a-b), which
216 suggests ongoing replication at the vgRNA clusters. In SR images, nsp12 localized in small sparse
217 puncta (d < 50 nm) that were scattered within and next to the vgRNA clusters at both time points
218 (Fig. 3c-d). Because nsp12 puncta are well separated from each other, and oligomerization is not
219 expected[22,23,25], each nanoscale punctum is likely to represent a single replicating enzyme. On
220 average, we detected 2.5 nsp12 puncta per vgRNA cluster at 6 hpi and 7.6 at 24 hpi (Fig. 3g).

221 Interestingly, in contrast to vgRNA but similar to dsRNA, the total nsp12 amount does not
222 significantly increase (Extended Data Fig. 2e) and its nanoscale localization pattern stays the same
223 as infection progresses from 6 to 24 hpi (Fig. 3c-d). This suggests that the growth of vgRNA clusters
224 arises from relatively constant small numbers of replication components between 6 and 24 hpi
225 highlighted by the constant amount of dsRNA and RdRp. Bivariate cross-correlation functions
226 calculated between nsp12 and vgRNA localizations peaked at 0 nm indicating association of these
227 two targets at both 6 and 24 hpi (Fig. 3e-f). Since vgRNA clusters colocalize with the catalytic
228 subunit of RdRp, we conclude that vgRNA clusters combined with the nearby RdRp enzymes and
229 dsRNA highlight ROs that act as centers for replication and transcription of SARS-CoV-2.

230

231

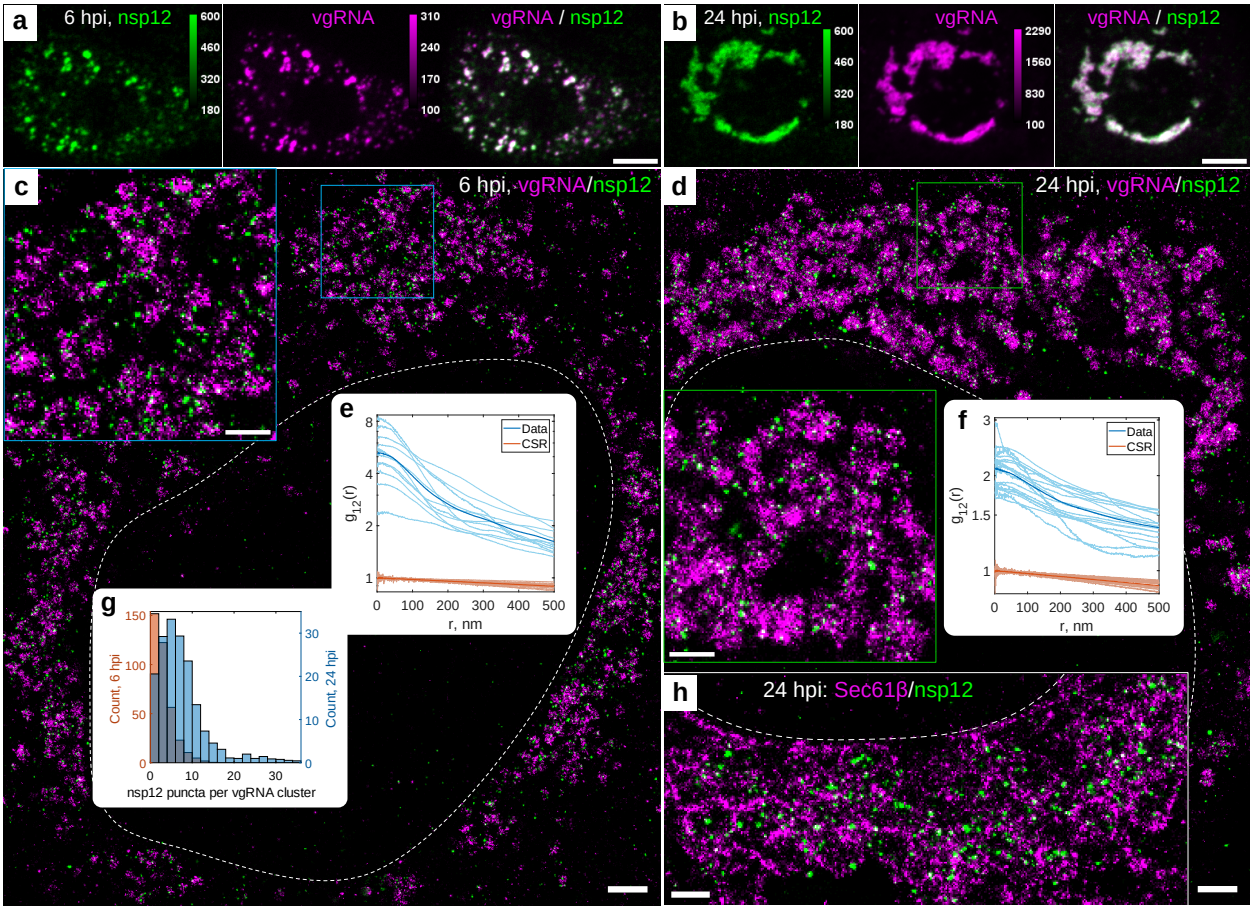

Fig. 3: Association of SARS-CoV-2 replication enzyme with vgRNA clusters

a-**b**, Representative confocal images of SARS-CoV-2 infected cells display DL colocalization between nsp12, the catalytic subunit of RdRp (green) and vgRNA (magenta) at both 6 hpi (**a**) and 24 hpi (**b**). **c**-**d**, Representative SR images of SARS-CoV-2 infected cells indicate nanoscale association between nsp12 and vgRNA at both 6 hpi (**c**) and 24 hpi (**d**). Insets show magnified images of corresponding regions in colored boxes. **e**-**f**, Bivariate pair-correlation functions peak at r = 0 nm indicating association between nsp12 and vgRNA. **g**, Number of nanoscale puncta of nsp12 per vgRNA cluster. **h**, SR image of nsp12 with Sec61β suggests encapsulation of nsp12 within ER-derived membranes. Scale bars, 10 µm (**a**-**b**), 1 µm (**c**-**d**), 500 nm (**h** and insets in **c**-**d**). Dashed lines in **c**, **d** and **h** indicate the edge of the cell nucleus.

vgRNA clusters are enclosed in ER-derived membranous organelles

Coronaviruses are thought to transform the host ER into replication-permissive structures, such as convoluted membranes and DMVs[3,26,27]. To investigate the relation of vgRNA clusters with cellular ER, we immunofluorescently labelled Sec61β, an ER membrane protein[28], in Vero E6 cells

248 stably expressing Sec61β-GFP[15]. Confocal images of these cells show the appearance of Sec61β
249 spots that colocalize with vgRNA against the mostly unaltered ER background at 6 hpi (Fig. 4a). At
250 24 hpi, however, substantial amounts of Sec61β accumulate close to the perinuclear vgRNA
251 clusters, while the ER tubules outside these regions become poorly visible (Fig. 4a), consistent
252 with the virus-induced rearrangement of the ER and the inhibition of host gene expression by
253 SARS-CoV-2[29].

254 In SR, we observe encapsulation of the vgRNA clusters by ring-like structures of the altered ER at
255 6 hpi (Fig. 4b, Extended Data Fig. 4). As infection progresses, the ER-derived ring- or sphere-like
256 structures grow to accommodate larger vgRNA clusters at 24 hpi (Fig. 4b, Extended Data Fig. 5).
257 Pair-correlation functions peak at the distance of the typical radius of vgRNA clusters indicating
258 nanoscale anti-correlation compatible with the ER-derived encapsulation of vgRNA (Fig. 4c).
259 dsRNA (Fig. 4b, Extended Data Fig. 6) and nsp12 (Fig. 3h) are also found to be encapsulated by
260 the same remodeled ER membranes suggesting that vgRNA, dsRNA and RdRp are all located
261 within the same ER-derived replication organelles.

262 To further confirm that these clusters are surrounded by membranes, we used a (d)STORM-
263 compatible general membrane marker CellMask Deep Red[30]. This dye broadly stains cellular
264 membranes, including the nuclear envelope, the mitochondrial membranes, and SARS-CoV-2
265 virions at the plasma membrane (Extended Data Fig. 7). The nanoscale image contrast with
266 CellMask Deep Red is poorer than specific protein labelling of the Sec61β ER label due to
267 background from membranes of different cellular organelles. Nevertheless, in the perinuclear
268 region of infected cells, we observed the appearance of a complex membranous network that
269 anti-correlates with vgRNA and dsRNA, with visible encapsulation of vgRNA and dsRNA clusters
270 (Extended Data Fig. 7, 9). Taken together, these findings indicate that the vgRNA-dsRNA-RdRp
271 clusters are located inside membrane-bound replication organelles (ROs) that originate from
272 altered host ER transformed by SARS-CoV-2.

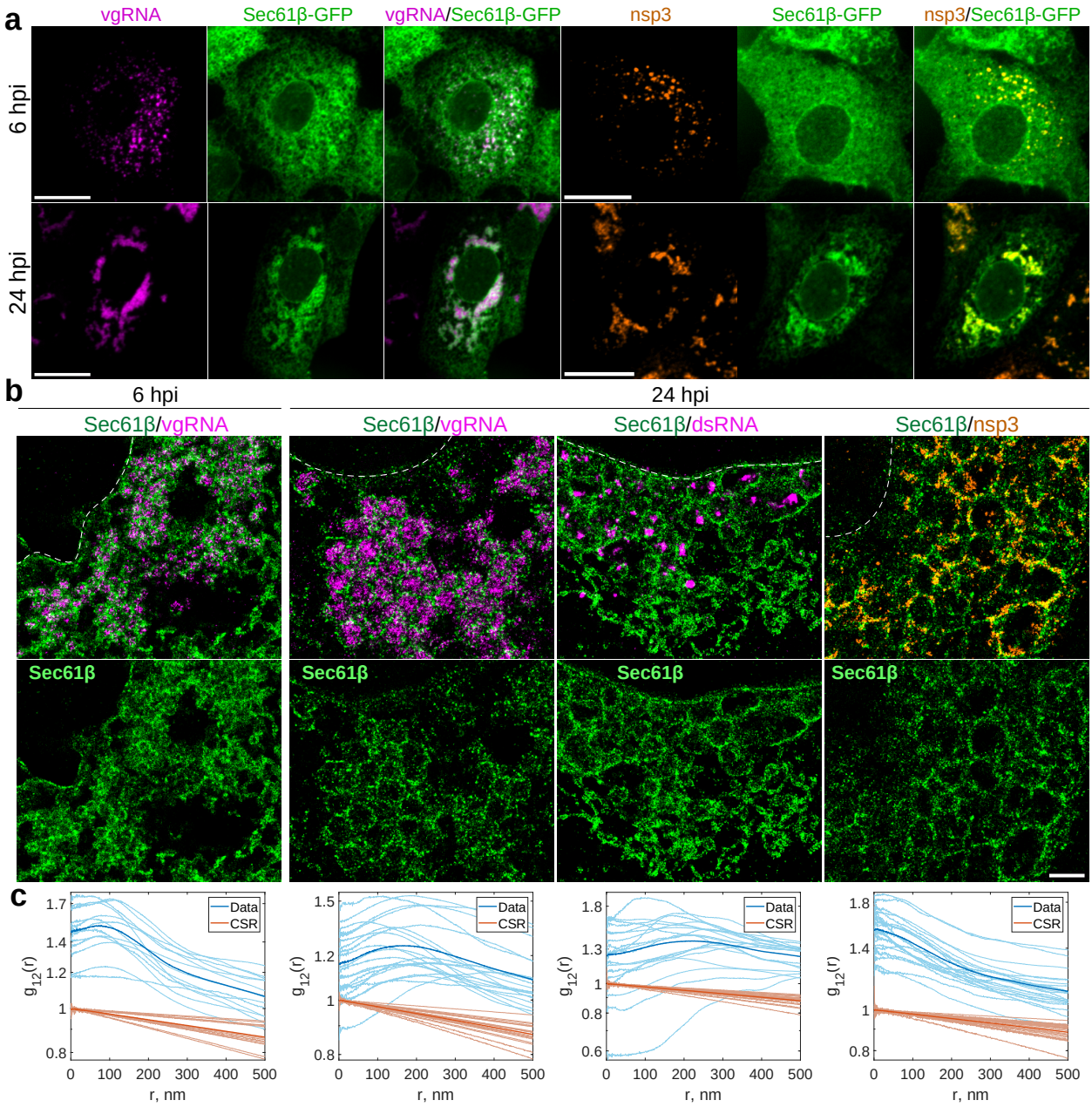

Fig. 4: vgRNA clusters are encapsulated in membranes of remodeled ER

a, Representative confocal images of SARS-CoV-2 infected cells indicate an appearance of dense perinuclear foci of Sec61β ER labelling at 24 hpi that colocalizes with vgRNA and nsp3. **b**, SR images reveal concentric organization of Sec61β around vgRNA and dsRNA and colocalization of Sec61β with nsp3. **c**, Bivariate pair-correlation functions indicate anti-correlation of Sec61β with vgRNA and dsRNA and association of Sec61β with nsp3. Scale bars, 20 µm (**a**) and 1 µm (**b**). Dashed lines in **b** indicate the position of the cell nucleus.

282 *Nsp3 localizes at the surface of SARS-CoV-2 replication organelles*

283 Because the nsp3 protein of betacoronaviruses is essential for the DMV formation[31,32], and nsp3
284 is a constituent of a DMV molecular pore[16], we proceeded to localize this non-structural protein
285 to relate the ROs to the SARS-CoV-2-induced DMVs. At DL resolution, nsp3 labelling adopts a
286 pattern that colocalizes with vgRNA at both 6 and 24 hpi, similarly to dsRNA and nsp12 (Fig. 5a,
287 f). SR imaging of these cells, however, revealed striking nanoscale positioning of nsp3. At 6 hpi,
288 sparse nsp3 can be found surrounding isolated vgRNA clusters (Fig. 5c-d), while larger nsp3
289 aggregates are situated amidst bunched vgRNA clusters (Fig. 5e). At 24 hpi, nsp3 localizes at the
290 borders of the large vgRNA clusters, encircling them in incomplete rings and forming a partial
291 perinuclear network (Fig. 5g, i, j). Similar nsp3 arrangements can be observed in relation to dsRNA
292 (Extended Data Fig. 8).

293 The anti-correlation of vgRNA with nsp3 and dsRNA with nsp3 (Fig. 5, Extended Data Fig. 8) closely
294 resemble the pattern observed with vgRNA and dsRNA with Sec61β (Fig. 4, Extended Data Fig. 6),
295 suggesting that nsp3 may also be localized at the ER-derived membranous surface of the ROs. To
296 further confirm this hypothesis, we co-imaged nsp3 with Sec61β and CellMask (Fig. 4, Extended
297 Data Fig. 9, Supplementary Fig. S1). The SR images and the pair-correlation analysis indicated
298 colocalization between nsp3 and both membrane markers at both time points (Fig. 4b-c,
299 Extended Data Fig. 9, Supplementary Fig. S1), confirming that nsp3 localizes on the membranes
300 encircling the SARS-CoV-2 ROs.

301 Besides these characteristic localization patterns of nsp3, we observed a few cells with two
302 different phenotypes at 24 hpi, one with an ER-like network that occupies large regions in the
303 cytoplasm (Extended Data Fig. 10a), and another one with nsp3 densely diffused throughout the
304 whole cytoplasm (Extended Data Fig. 10b). The ER-like network may represent nsp3 proteins
305 being heavily translated on ER membrane, while nsp3 proteins found outside the perinuclear
306 region are less likely to be associated with the SARS-CoV-2 replication process and might
307 represent other nsp3 functions, such as a papain-like proteolytic function[33] or post-translational
308 modification of host proteins[34], which can become objects of future SR studies.

309 The localization of nsp3 at the surface of isolated vgRNA-dsRNA clusters at 6 hpi is consistent with
310 the localization of molecular pores on the DMV membrane observed by cryo-EM[16]. At late
311 infection times, DMVs have been observed to merge into vesicle packets (VPs)[5] that are also likely
312 to contain pores, however molecular pores in the VP membranes have not yet been studied in
313 detail to our knowledge. Nevertheless, previous studies report that in late infection the
314 perinuclear region becomes filled with DMVs and VPs[26] that strongly resemble the ROs reported
315 here. The size of vgRNA clusters at 6 hpi and at 24 hpi from our data is similar to the previously
316 reported size of DMVs and VPs, correspondingly[5]. Taken together, our results provide evidence
317 that vgRNA accumulates, possibly in DMVs at 6 hpi and in VPs at 24 hpi. dsRNA clusters occur
318 within the same vesicles but occupy distinct parts of them. Our data are consistent with the
319 picture that SARS-CoV-2 RNA is replicated and transcribed within these DMVs and VPs as
320 highlighted by the proximal localizations of RdRp.

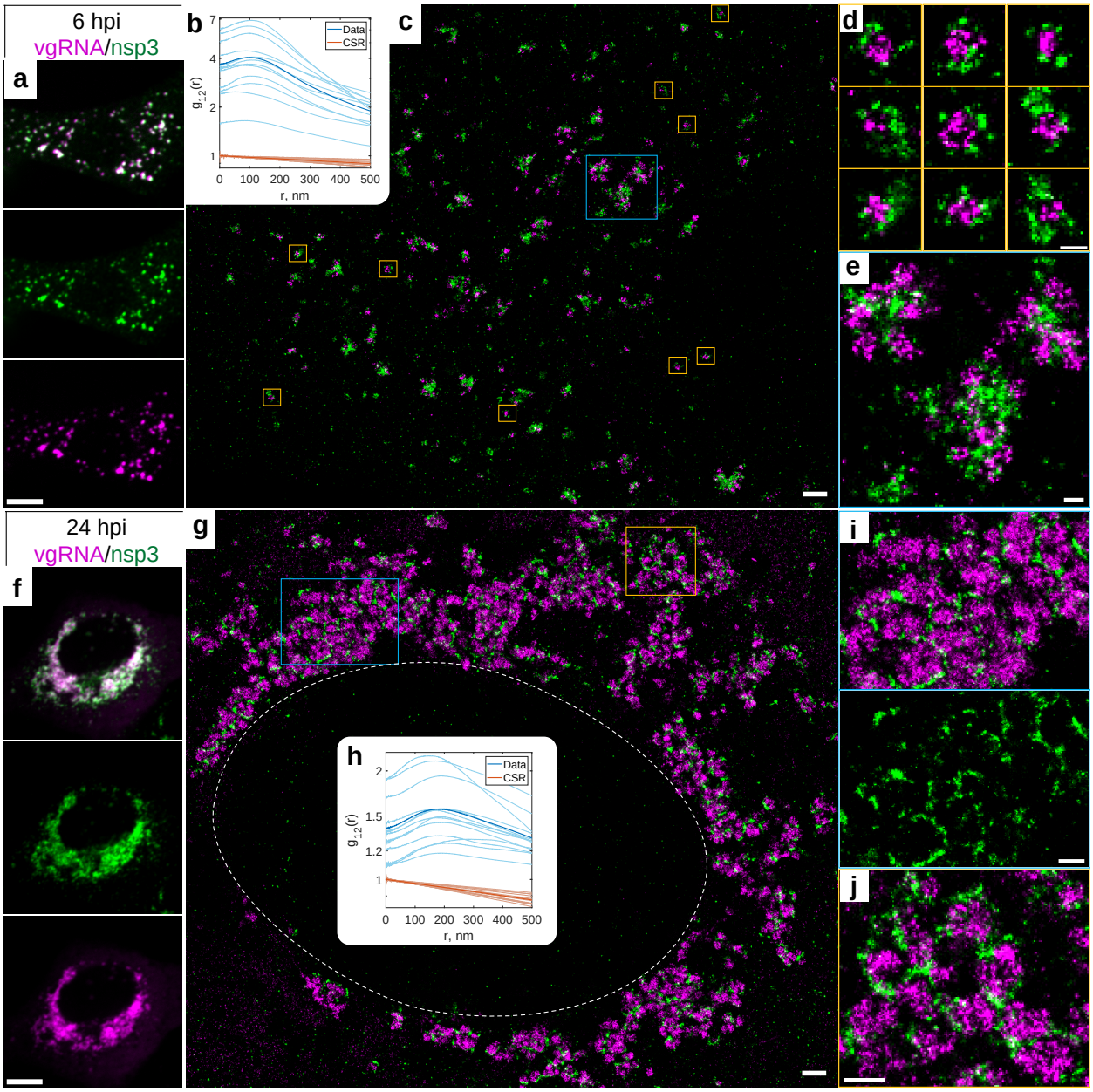

Fig. 5: Nsp3 localizes at the surface of vgRNA clusters

a, Representative confocal images of a SARS-CoV-2 infected cell display DL colocalization between punctate vgRNA and nsp3 labeling at 6 hpi. **b**, Bivariate pair-correlation functions calculated between the SR localizations of vgRNA and nsp3 indicate nanoscale anti-correlation of these targets at 6 hpi. **c**, Representative SR image of a SARS-CoV-2 infected cell at 6 hpi. **d**, Zoomed-in images of selected vgRNA particles (yellow boxes in **c**) indicate the localization of nsp3 at the surface of the vgRNA clusters. **e**, Magnified region with aggregates of vgRNA clusters (blue box in **c**) displays dense nsp3 localization in the core of these aggregates. **f**, Confocal images indicate that vgRNA and nsp3 occupy approximately the same regions in a SARS-CoV-2 infected cell at 24 hpi. **g**, Representative SR image of a SARS-CoV-2 infected cell at 24 hpi. **h**, Bivariate pair-

correlation functions indicate nanoscale anti-correlation between vgRNA and nsp3 at 24hpi. **i-j**, Magnified regions of the SR image (colored boxes in **g**) show that nsp3 localizes in interstitial regions or encapsulates vgRNA clusters. Scale bars, 10 µm (**a**, **f**), 1 µm (**c**, **g**), 500 nm (**i**, **j**), 200nm (**d**, **e**). Dashed line in **g** indicates the position of the cell nucleus.

Discussion

Previous biochemical and EM studies allowed researchers to build models of the intracellular life cycle of SARS-CoV-2[35-37]; however, precise localization of specific viral proteins and RNA molecules is challenging due to lack of specific contrast in EM and low resolution in DL fluorescence microscopy. SR fluorescence microscopy is well suited for coronavirus studies in cells as it provides both specific contrast and high resolution (~20 nm and below depending upon photons collected[38]). However, to date few studies have employed this method for coronavirus biology[15], even less for SARS-CoV-2[27,39,40], and none of them focused on the SARS-CoV-2 replication process in detail. Here we apply SR fluorescence microscopy to precisely localize the key players of SARS-CoV-2 replication at different timepoints in infected cells. Building upon a previously developed method for simultaneous labelling of coronavirus vgRNA with dsRNA and protein immunofluorescence[15], and using improved fixation and multi-color SR imaging protocols (see Methods), we obtain and quantify the appearance and molecular compositions of ROs of SARS-CoV-2 in cells at different stages of infection.

In this study, our results taken together depict a compelling and novel picture of ROs containing various molecules including vgRNA, dsRNA, RdRp, nsp3, and ER membrane (Fig. 6). In this model, we compare organization of ROs at early and late stages of infection and show how specific RNA and protein molecules are spatially organized in ROs. Compared to the 229E case, SARS-CoV-2 appears to generate more complex clusters of vgRNA, and with the additional imaging of relevant targets in this study, the structural importance of ROs is now clear.

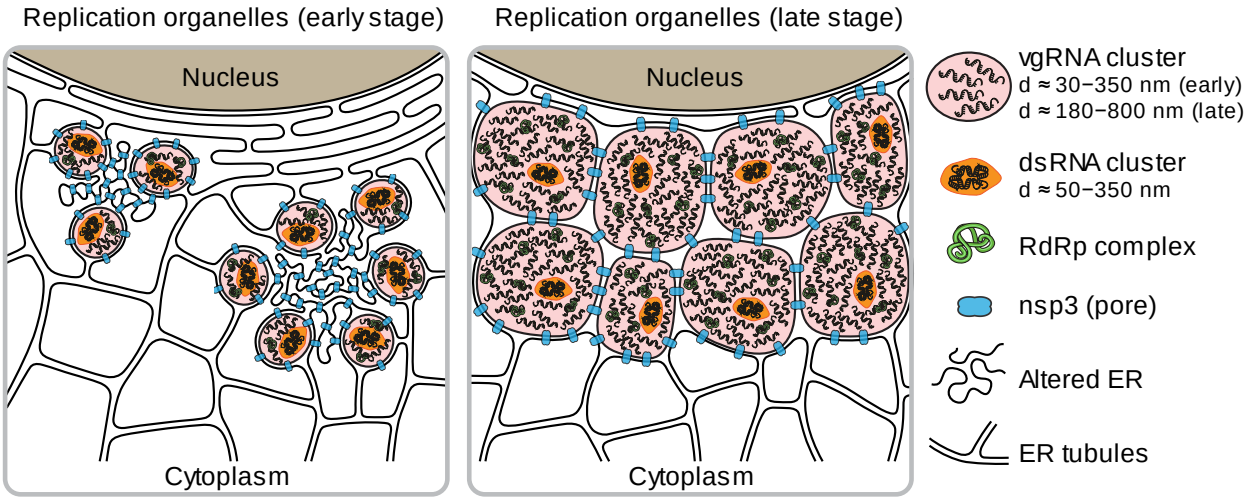

Fig. 6: Proposed model for SARS-CoV-2 replication organelles containing various RNA and protein molecules at early and late stages of infection.

The detailed intracellular localization of the central SARS-CoV-2 component, vgRNA, has remained vague in the literature. Our RNA FISH method[15] targets specific sequences in vgRNA (Fig. 1a) and detects single vgRNA molecules (Extended Data Fig. 1, 3a), allowing counting of the number of vgRNA molecules within specific regions (Extended Data Fig. 3b-c). We find for the first time that most cellular vgRNA localizes into dense clusters of an approximately round shape that grow and migrate to the perinuclear region as infection time increases. We show that these clusters appear confined in membranous vesicles derived from ER as emphasized by the localization of Sec61β and CellMask at their surface (Fig. 4b, Extended Data Fig. 4, 5, 9). From comparison with earlier EM images[5,16,26] and from nsp3 localization at their surface[16] (Fig. 5), we can conclude that these vesicles are most likely DMVs at an early-mid infection time that grow and merge into VPs as infection progresses.

Previously, metabolic radioactive labelling was used to localize newly synthesized RNA in SARS-CoV-1 and MERS-CoV-infected cells to DMVs[4]. However, metabolic labelling could only localize a fraction of viral RNA molecules with little sequence specificity and with a background of newly transcribed cellular RNA. Here, we specifically label vgRNA of SARS-CoV-2 for SR microscopy and

380 show that it also localizes in patterns that suggest confinement in DMVs, confirming the earlier
381 findings on SARS-CoV-1 and MERS-CoV[4].

382 Previous studies also reported presence of dsRNA in DMVs of SARS-CoV-1[3] and SARS-CoV-2[5]. EM
383 images of DMVs often display a complex filamentous network in their interior, that was attributed
384 to viral RNA molecules[5]. However, the exact type of these RNAs was not determined due to the
385 absence of specific labelling. As one might expect, single-stranded vgRNA can form a secondary
386 structure that includes many short dsRNA fragments *e.g.*, in stem loops[41,42]. This makes it difficult
387 to distinguish between viral dsRNA and vgRNA by measuring the diameter of the filaments, taking
388 into account that the detection probability of ssRNA might be lower due to a decreased EM
389 contrast for ssRNA than for dsRNA. Reported abundant branching of filaments in DMVs[5], however,
390 is typical for ssRNA secondary structures[43]. Indeed, there was evidence in the literature about
391 presence of both dsRNA and vgRNA in DMVs; however, to our knowledge, there was no
392 simultaneous observation of both vgRNA and dsRNA within the same DMVs.

393 Here we use the J2 anti-dsRNA antibody that recognizes only long dsRNA fragments (≥ 40bp) with
394 no detection of the ssRNA secondary structures[44,45]. Two-color SR imaging revealed for the first
395 time that most dsRNA and vgRNA are located within the same DMVs and VPs, occupying distinct
396 regions of these vesicles, and adopting an anti-correlation pattern at short distances ($r < 100$ nm)
397 at 24 hpi (Fig. 2). A similar nanoscale anti-correlation has been observed in the 229E coronavirus
398 but the DMVs or ROs were not specifically labelled in that study[15]. Another novel observation is
399 the relatively constant amount of dsRNA and little change in dsRNA cluster size between 6 and
400 24 hpi despite the huge change in the vgRNA landscape (Fig. 2).

401 It has been proposed that the RdRp complex of SARS-CoV-1 is located at convoluted membranes
402 and inside DMVs based on immunogold labelling of nsp8[3]. However, nsp8 has intracellular
403 functions other than as an RdRp accessory subunit[46,47] that might be exercised at the convoluted
404 membranes. Here we label the catalytic RdRp subunit, nsp12[22], and find that it mostly localizes
405 to the vgRNA clusters at both 6 and 24 hpi (Fig. 3), suggesting that SARS-CoV-2 replication and
406 transcription occurs preferentially in the vgRNA-filled ROs, where dsRNA resides as well.

407 Nsp3 of betacoronaviruses (SARS-CoV-1, MERS-CoV and MHV) was previously localized to the
408 convoluted membranes and to the DMV membranes using immuno-EM[3,4,48,49] and cryo-ET[16];
409 however, these studies were limited to early-mid infection at 8-12 hpi. In our study, we report
410 two localization patterns of nsp3 of SARS-CoV-2 at 6hpi: 1) sparse nsp3 at the surface of isolated
411 vgRNA-dsRNA clusters (Fig. 5d, Extended Data Fig. 8a); 2) dense nsp3 within the accumulations
412 of vgRNA-dsRNA clusters (Fig. 5e, Extended Data Fig. 8a). While the first pattern most likely
413 corresponds to the RO/DMV membranes considering the role of nsp3 as a DMV pore[16], the
414 second one resembles a pattern found in other coronaviruses that was attributed to the
415 convoluted membranes[3,4,50]. Convoluted membranes are typically found within dense groups of
416 DMVs in early-mid infection[3,4] and localization of nsp3 on them might represent early steps of
417 viral transformation of ER into DMVs. We found this nsp3 pattern anti-correlated with vgRNA (Fig.
418 5c, e) and with dsRNA (Extended Data Fig. 8a-b), suggesting little to no vgRNA or dsRNA at the
419 convoluted membranes, in line with previous studies on other coronaviruses[4].

420 At 24 hpi, we did not observe these early infection patterns of nsp3 localization. Instead, we show
421 for the first time that at 24 hpi, nsp3 densely localizes at the membranes that separate large
422 vgRNA clusters and grows into a considerable perinuclear network that contains the ROs (Fig. 5g,
423 i-j, Extended Data Fig. 8c). Since the molecular pores of VPs have not yet been investigated in
424 detail, we can speculate that this late infection nsp3 pattern corresponds to the pores of VPs that
425 should also be much denser than those of isolated DMVs, considering the increased density of
426 nsp3 labelling. Additional rare phenotypes of nsp3 localization that we also report for the first
427 time (Extended Data Fig. 10) illustrate the variability of SARS-CoV-2 infection course and should
428 lead to further research on the other intracellular functions of this viral protein.

429 Taken together, we investigated several key factors of SARS-CoV-2 replication: vgRNA, dsRNA,
430 RdRp and nsp3 inside infected cells with SR microscopy for the first time. We discovered and
431 characterized perinuclear clusters of vgRNA and demonstrated by RdRp labelling that they
432 associate with SARS-CoV-2 ROs. We found that the ROs also contain dsRNA and are encapsulated
433 in ER-derived membranes. Using SR data on nsp3, we conclude that these virus-induced
434 organelles correspond to DMVs.

435 This study expands the knowledge of the biology of coronaviruses and opens new possibilities for
436 therapeutics against SARS-CoV-2. Careful examination of the organization of replication
437 organelles may provide new avenues to target the organelles to disrupt SARS-CoV-2 replication
438 and transcription. Examining localization patterns for different viral variants or in different host
439 cells will be useful to broaden understanding of the viral infection. It will also be important to
440 examine how the structures reported in this study change upon the addition of drug treatments.
441 Our imaging approach may also offer insights into long COVID by investigating cells that are
442 infected by SARS-CoV-2 that may still contain RO-like structures after symptoms disappear.

443

444

445 **Methods**

446 *Antibodies*

447 Primary antibodies and the optimal dilutions and concentrations used are as follows: goat
448 polyclonal anti-spike S2 (Novus Biologicals, AF10774-SP, 1:20, 10 µg/mL), mouse monoclonal anti-
449 dsRNA (SCICONS, 10010200, 1:200, 5 µg/mL), rabbit polyclonal anti-RdRp/nsp12 (Sigma-Aldrich,
450 SAB3501287-100UG, 1:500, 2 µg/mL), mouse monoclonal anti-nucleocapsid (Thermo Fisher,
451 MA5-29981, 1:500, 2 µg/mL), rabbit polyclonal anti-nsp3 (Thermo Fisher, PA5-116947, 1:134, 5
452 µg/mL), sheep polyclonal anti-GFP (Bio-Rad, 4745-1051, 1:1000, 5 µg/mL), and rabbit polyclonal
453 anti-GFP (Novus Biologicals, NB600-308SS, 1:163, 5 µg/mL). Secondary antibodies and the
454 optimal dilutions and concentrations used are as follows: AF647-conjugated donkey anti-mouse
455 IgG (Thermo Fisher, A-31571, 1:500, 4 µg/mL), AF647-conjugated donkey anti-rabbit IgG (Thermo
456 Fisher, A-31573, 1:500, 4 µg/mL), AF647-conjugated donkey anti-sheep IgG (Thermo Fisher, A-
457 21448, 1:500, 4 µg/mL), CF568-conjugated donkey anti-goat IgG (Sigma-Aldrich, SAB4600074-
458 50UL, 1:500, 4 µg/mL), CF568-conjugated donkey anti-rabbit IgG (Sigma-Aldrich, SAB4600076-
459 50UL, 1:500, 4 µg/mL), CF568-conjugated donkey anti-mouse IgG (Sigma-Aldrich, SAB4600075-
460 50UL, 1:500, 4 µg/mL), and CF568-conjugated donkey anti-sheep IgG (Sigma-Aldrich,
461 SAB4600078-50UL, 1:500, 4 µg/mL).

462

463 *Culture of cell lines*

464 The Vero E6 cells (African green monkey kidney epithelial cells, ATCC, CRL-1586), HEK293T cells
465 (human embryonic kidney epithelial cells, ATCC, CRL-3216), and Vero E6-TMPRSS2 cells were
466 cultured in Dulbecco's modified Eagle medium (DMEM) with GlutaMAX, 25 mM D-Glucose, and
467 1 mM sodium pyruvate (Gibco, 10569010) in 10% FBS (Sigma-Aldrich, F0926) at 37°C and 5% CO2
468 in a humidified incubator. Cell lines were not authenticated after purchase prior to use. For Vero
469 E6-TMPRSS2, Geneticin (G418) was added at a final concentration of 1mg/ml.

470

471 *Lentivirus production for ER labeling with Sec61β*

472 To produce lentivirus, HEK293T cells were cultured in 10-cm dishes and transiently transfected
473 with 9 µg lentiviral plasmid pLV-ER-GFP (Addgene, 80069, a gift from Pantelis Tsoulfas), 8 µg
474 pCMV-dR8.91, and 1 µg PMD2.G packaging plasmids using 25 µL TransIT-LT1 Transfection Reagent
475 (Mirus, MIR 2306). After 72 h of transfection, supernatant was filtered through 0.45 µm filters,
476 concentrated using Lentivirus Precipitation Solution (ALSTEM, VC100) at 4°C overnight, and
477 centrifuged at 1,500x g for 30 min at 4°C to collect virus pellets. The virus pellets were
478 resuspended in cold DMEM for storage at -80°C for transduction of cells.

479

480 *Generation of stable cell line*

481 To generate a Vero E6 cell line stably expressing Sec61β-GFP, $2x10^5$ Vero E6 cells were seeded in
482 one well of a 6-well plate and infected with one quarter of concentrated lentivirus expressing pLV-
483 ER-GFP produced from one 10-cm dish of HEK293T cells while seeding. After two days incubation,
484 monoclonal cells expressing GFP were sorted out using a SONY SH800S sorter. These transduced
485 cells were only used for ER imaging; all other experiments used wild type (WT) cells.

486

487 *SARS-CoV-2 viral stocks preparation*

488 The SARS-CoV-2 WA 1, isolate USA-WA1/2020 (NR-52281, BEI Resources) was passaged 3 times
489 in Vero E6-TMPRSS2 cells as previously described[51,52]. Briefly, a Vero E6-TMPRSS2 monolayer was
490 infected with virus obtained from BEI; post 72 hours of infection (hpi), P1 virus-containing tissue
491 culture supernatants were collected and stored at -80°C. Following titration, P1 virus stock was
492 used to generate a P2 stock by infecting Vero E6 TMPRSS2 monolayers with multiplicity of
493 infection (MOI) of 0.0001 for 72 hours. P2 virus was passaged again in Vero E6-TMPRSS2 cells to
494 obtain P3 stock. Viral titers were determined by standard plaque assay on Vero E6 cells.

495

496 *Infection of cells by SARS-CoV-2*

497 Vero E6 cells previously cultured in 8-well µ-slides were infected in the BSL3 facility with SARS-
498 CoV-2 WA 1 (USA212 WA1/2020) in triplicates (MOI=0.5 SARS-CoV-2 WA1 (P3)) at an MOI of 2 for
499 6 hpi and MOI of 0.2 for 24 hpi. After 6 and 24 hrs of incubation, cells were washed with PBS and
500 fixed by 4% PFA (Electron Microscopy Sciences #15710) and 0.1% glutaraldehyde (Electron
501 Microscopy Sciences #16350) in PBS for 1 hour and removed from BSL3 for further processing. All
502 work involving viral stock preparation and infection using WT SARS-CoV-2 was conducted at the
503 high containment BSL3 facility of Stanford University according to CDC and institutional
504 guidelines. All the experiments were performed using a P3 SARS-CoV-2 USA-WA1/2020,
505 containing 100% WT population with no deletion in the spike multi-basic cleavage site.

506

507 *Synthesis of the RNA FISH probes*

508 vgRNA FISH probes targeting the ORF1a region of SARS-CoV-2[17] were ordered with 5AmMC6
509 modifications from Integrated DNA Technologies, Inc. in plate format of 25 nmol scale with
510 standard desalting. Each probe was dissolved in water to a final concentration of 100 µM. The
511 same set of probes was combined with equal volumes of each probe to get a stock of 100 µM
512 mixed probes. The mixed probes were further desalted using ethanol precipitation. Briefly, 120
513 µL 100 µM probes were mixed with 12 µL 3 M sodium acetate (pH 5.5), followed by 400 µL
514 ethanol. After precipitation at -80C overnight, probes were pelleted through centrifugation at
515 12,000x g for 10 min at 4°C, washed with precooled 70% (vol./vol.) ethanol three times, air dried,
516 and dissolved in water to make a 100 µM solution of probes. Then, 18 µL 100 µM probes were
517 mixed with 2 µL 1 M $NaHCO_3$ (pH 8.5), followed by 100 µg Alexa Fluor™ 647 succinimidyl ester
518 (NHS) (Invitrogen, A37573) or CF568 succinimidyl ester (NHS) (Biotium, 92131) dissolved in 2 µL
519 dry DMSO (Invitrogen, D12345). The mixture was incubated for 3 days at 37C in the dark for
520 conjugation and purified for 3 rounds using Monarch PCR & DNA Cleanup Kit (5 µg) (NEB, T1030S)
521 following the manufacturer's instructions. The estimated labeling efficiency of probes was
522 calculated using the following equation:

523 $$Modification\ ratio = \frac{20}{(A_{base} \times \varepsilon_{dye})\ /\ (A_{dye} \times \varepsilon_{base})}$$

524 where ε_{dye} is 239,000 $cm^{-1}M^{-1}$, ε_{base} is 8,919 $cm^{-1}M^{-1}$, A_{base} is the absorbance of the nucleic acid at
525 260 nm, and A_{dye} is the absorbance of the dye at 650 nm. For the probes labeled with CF568, ε_{dye}
526 is 100,000 $cm^{-1}M^{-1}$, ε_{base} is 8,919 $cm^{-1}M^{-1}$, A_{base} is the absorbance of the nucleic acid at 260 nm,
527 and A_{dye} is the absorbance of the dye at 562 nm.

528

529 *RNA FISH, immunofluorescence (IF), and CellMask staining*

530 Fixed cells from BLS3 as described above were washed twice with a freshly prepared 0.1% $NaBH_4$
531 solution at room temperature for 5 min, and washed with PBS three times. For staining without
532 CellMask (Thermo Fisher, C10046), cells were permeabilized in 70% ethanol at 4°C overnight. For
533 CellMask staining, cells were permeabilized in 0.1% Triton X-100 at room temperature for 30 min.

534 For RNA FISH staining, permeabilized cells were washed with 200 µL Wash Buffer A [40 µL Stellaris
535 RNA FISH Wash Buffer A (LGC Biosearch Technologies, SMF-WA1-60), 20 µL deionized formamide,
536 140 µL H2O] at room temperature for 5 min, and incubated with 110 µL Hybridization Buffer [99
537 µL Stellaris RNA FISH Hybridization Buffer (LGC Biosearch Technologies, SMF-HB1-10), 11 µL
538 deionized formamide] containing 1.1 µL 12.5 µM vgRNA FISH probes for 4 hours at 37°C in the
539 dark. Then cells were washed with Wash Buffer A for 30 min at 37°C in the dark, washed with
540 Wash Buffer A containing DAPI for 30 min at 37°C in the dark, and stored in Wash Buffer B (LGC
541 Biosearch Technologies, SMF-WB1-20) for imaging. DAPI was only added to the samples for
542 confocal imaging and not added to the samples for SR imaging.

543 For IF staining with antibodies, permeabilized cells were washed with PBS twice, incubated with
544 3% BSA in PBS at room temperature for 30 min, and incubated with primary antibodies in PBS at
545 37°C for 1 hour. After incubation with primary antibodies, cells were washed twice with PBST
546 buffer (0.1% Tween-20 in PBS) at room temperature for 5 min, washed with PBS once, incubated
547 with secondary antibodies in PBS at room temperature for 30 min, washed with PBST buffer three
548 times at room temperature for 5 min, and stored in PBS for imaging.

549 For simultaneous RNA FISH and IF staining, permeabilized cells were washed with 200 µL Wash
550 Buffer A at room temperature for 5 min, and incubated with 110 µL Hybridization Buffer (99 µL

551 Stellaris RNA FISH Hybridization Buffer, 11 µL deionized formamide) containing 1.1 µL 12.5 µM
552 vgRNA FISH probes, 1 U/µL RNase inhibitor (NxGen, F83923-1), and primary antibodies for 4 hours
553 at 37°C in the dark. Then cells were washed with 2xSSC buffer once, washed with Wash Buffer A
554 containing secondary antibodies for 30 min at 37°C in the dark, washed with Wash Buffer A for
555 30 min at 37°C in the dark, washed with Wash Buffer B once, and stored in Wash Buffer B for
556 imaging. For CellMask staining, several more steps were performed from here. Cells were washed
557 with PBS once, stained with 1:20k CellMask and 1 U/µL RNase inhibitor in PBS for 20 min at room
558 temperature in the dark, and washed with PBS three times before imaging.

559

560 *RNA FISH and IF staining of purified virions*

561 8-well µ-slides (ibidi, 80827-90) were first treated with poly-D-lysine solution (Thermo Fisher,
562 A3890401) at 4°C overnight. Then in the BSL3 facility, the poly-D-lysine solution was removed and
563 150 µL SARS-CoV-2 WA1 (P3) virus solution of titer 1.82×10^5 PFU/mL was added into one well of
564 poly-D-lysine-treated 8-well µ-slides for incubation at 4°C for 24 hours to coat the virions onto
565 the surface of the well. After incubation, the medium containing virions was removed and the
566 well was washed with PBS twice. Virions on the surface of the well were fixed with 4% PFA in PBS
567 for 1 hour at room temperature and the sample was removed from BSL3. The sample was washed
568 twice with a freshly prepared 0.1% $NaBH_4$ solution at room temperature for 5 min, and then
569 washed with PBS three times. The fixed virions were permeabilized in 70% ethanol at 4°C
570 overnight and washed with PBS twice. For the group with Proteinase K digestion, virions were
571 incubated with 0.2 mg/mL Proteinase K (NEB #P8107S) in 120 µL PBS at 37°C for 30 min and
572 washed with PBST buffer three times. Virions were washed with Wash Buffer A once and
573 incubated with 110 µL Hybridization Buffer (99 µL Stellaris RNA FISH Hybridization Buffer, 11 µL
574 deionized formamide) containing 1.1 µL 12.5 µM vgRNA FISH probes, 1 U/µL RNase inhibitor, and
575 primary antibodies for 4 hours at 37°C in the dark. Then virions were washed with 2xSSC buffer
576 once, washed with Wash Buffer A containing secondary antibodies for 30 min at 37°C in the dark,
577 washed with Wash Buffer A for 30 min at 37°C in the dark, washed with Wash Buffer B once, and
578 stored in Wash Buffer B for imaging.

579

580 *Spinning disk confocal microscopy*

581 Confocal microscopy was performed at the Stanford University Cell Sciences Imaging Core Facility
582 with a Nikon TiE inverted spinning disk confocal microscope (SDCM) equipped with a
583 Photometrics Prime 95B camera, a CSU-X1 confocal scanner unit with microlenses, and 405 nm,
584 488 nm, 561 nm, and 642 nm lasers, using the 60x/1.27 NA PLAN APO IR water immersion
585 objective. Images were taken using NIS Elements software version 4.60 with Z stacks at 0.3 µm
586 steps. The camera pixel size of SDCM is 0.183 µm/pixel and the pinhole size is 50 µm. Only one Z
587 slice is used for all images shown.

588

589 *Analysis of confocal data*

590 To extract the intensity of vgRNA, dsRNA and RdRp in each infected cell (Extended Data Fig. 2),
591 the summation projection of each z stack was created by Fiji[53]. The intensity of each target species
592 in each cell was measured by Fiji, subtracting the background of the same color channel. The
593 infected cells were characterized manually into three types based on the morphology of vgRNA.
594 Type 1 shows scattered dot-like localization of vgRNA. Type 3 shows large clustered vgRNA. Type
595 2 contains features of both type 1 and type 3.

596

597 *Optimization of antibody concentrations*

598 We optimized the concentration of antibodies in this study by quantifying their signal-to-
599 background ratio (SBR), where the signal is the brightness of the IF labelling in the cells that
600 express the given target (virus-infected sample or cells expressing Sec61β-GFP), and the
601 background is the brightness in the negative control cells (not-infected or WT cells).

602 To optimize the concentration of primary antibodies against the viral targets, different
603 concentrations of the primary antibody were applied to stain Vero E6 cells in SARS-CoV-2-infected
604 and not-infected samples under a constant secondary antibody concentration (Supplementary

605 Fig. S2). To optimize the concentration of secondary antibodies, different concentrations of the
606 secondary antibody were applied to stain Vero E6 cells in infected (virus+) and not-infected
607 (virus−) samples under a constant primary antibody concentration (Supplementary Fig. S3). For
608 each cell, a 11 pixel x 11 pixel box was drawn in the region with brightest signal in the cell and the
609 mean intensity within that region was measured to represent the intensity of target antibody in
610 that cell. The SBR was calculated, after subtraction of the dark signal I_{dark}, using the following
611 equation:

612 $$SBR = \frac{< I_{virus+} - I_{dark} >}{< I_{virus-} - I_{dark} >}$$

613 To optimize the concentration of the anti-GFP antibodies, different concentrations of primary
614 antibody were applied to stain Vero E6 Sec61B-GFP cells and WT Vero E6 cells under a constant
615 secondary antibody concentration (Supplementary Fig. S2). For each cell, a 11 pixel x 11 pixel box
616 was drawn in the region with the brightest signal in the cell and the mean intensities of both the
617 GFP and the antibody signals within that region were measured after subtraction of the dark
618 signals. To account for the variable expression levels among different cells, the IF signal I_{IF} was
619 normalized by the GFP signal I_{GFP} within the given region. The SBR was calculated using the
620 following equation:

621 $$SBR = \frac{< I_{IF,Sec61B\text{-}GFP} / I_{GFP,Sec61B\text{-}GFP} >}{< I_{IF,WT} / I_{GFP,WT} >}$$

622

623 For the primary antibodies against GFP, nsp3, nucleocapsid, nsp12 and for the secondary antibody
624 for the dsRNA labelling, we chose the antibody concentration that produces the highest SBR as
625 the optimal concentration. For the primary antibodies against spike S2 and dsRNA and for the
626 secondary antibody for the spike S2 labelling, we chose the concentration that yields the second
627 highest SBR because it provides a significantly lower non-specific background with only a minor
628 decrease of the estimated SBR.

629

630 *Optical setup for SR microscopy*

631 (d)STORM SR microscopy was performed on a custom-built system (Supplementary Fig. S4),
632 consisting of a Nikon Diaphot 200 inverted microscope frame with an oil-immersion objective
633 60x/1.35 NA (Olympus UPLSAPO60XO) and a Si EMCCD camera (Andor iXon Ultra 897). We used
634 642 nm and 560 nm 1W continuous-wave (CW) lasers (MPB Communications Inc.) for excitation
635 of AF647 or CellMask and CF568, accordingly. For reactivation of fluorophores from the dark state
636 we used a 405 nm 50 mW CW diode laser (Coherent OBIS). All laser beams were expanded and
637 co-aligned in free space and coupled into a square-core multi-mode fiber with a shaker for speckle
638 reduction (Newport F-DS-ASQR200-FC/PC). The output tip of the fiber (200 x 200 μm^2 core size)
639 was imaged with a 10x/0.25 NA objective and magnified to achieve a square illumination region
640 of 47.6 x 47.6 μm^2 with a constant intensity in the sample image plane of the main objective. The
641 fluorescence was split from the excitation light with a multi-band dichroic mirror
642 (ZT405/488/561/640rpcv2, Chroma) and filtered with dichroic filters (ZET635NF, ZET561NF,
643 T690LPxxr, all Chroma). The fluorescence of AF647 and CellMask was additionally filtered with a
644 band-pass filter (ET685/70M, Chroma) and that of CF568 with a combination of 561LP and
645 607/70BP (Semrock, EdgeBasic and BrightLine). The sample image was focused with a tube lens
646 (f = 400 mm) on the EMCCD camera, providing a pixel size of 117 x 117 nm^2 in sample coordinates.

647 Axial drift was compensated with a custom Focus Lock system[54]. We used an 808 nm fiber-coupled
648 diode laser (Thorlabs S1FC808) whose output fiber tip was conjugated with the back focal plane
649 of the imaging objective, allowing changing the angle of this beam out of the objective by
650 translating the fiber tip (Supplementary Fig. S4). This inclined beam was partially reflected from
651 the coverslip-water interface and the reflected beam was focused with a cylindrical lens onto a
652 CMOS sensor (UI-3240CP-NIR, IDS Imaging). The 808 nm beam was aligned such that the image
653 of the reflected beam would shift laterally when the axial position of the sample changes. The
654 sample was mounted on two stacked piezo stages (U-780.DOS for coarse and P-545.3C8S for fine
655 movement, both Physik Instrumente). The position of the reflected beam image was recorded
656 when the sample was set at the desired Z position for imaging. During imaging, the Z-position of
657 the fine stage was directed to move proportionally to the shift of the reflected beam image from

658 the recorded position, compensating for Z-drift. The Focus Lock control code was programmed in
659 Matlab (MathWorks, Inc.).

660

661 *SR imaging procedure*

662 For (d)STORM, the sample chamber was filled with 300 µl of a photoblinking buffer consisting of
663 200 U/ml glucose oxidase, 1000 U/ml catalase, 10% w/v glucose, 200 mM Tris-HCl pH 8.0, 15 mM
664 NaCl and 50 mM cysteamine. The buffer was prepared using the following stock solutions[38]: 1)
665 4 kU/ml glucose oxidase (G2133, Sigma), 20 kU/ml catalase (C1345, Sigma), 25 mM KCl (P217,
666 Fisher), 4 mM TCEP (646547, Sigma), 50% v/v glycerol (BP229, Fisher) and 22 mM Tris-HCl pH 7.0
667 (BP1756, Fisher), stored at −20 °C; 2) 1 M cysteamine-HCl (30080, Sigma), stored at −20 °C; 3) 37%
668 w/v glucose (49139, Sigma) with 56 mM NaCl (S271, Fisher) and 0.74 M Tris-HCl pH 8.0
669 (J22638.AE, Fisher), stored at +4 °C. For samples with RNA FISH labelling, the buffer was
670 supplemented with 1 U/µl of an RNase inhibitor (302811, LGC Biosearch Technologies).

671 The SR imaging started with a DL image of cells from each fluorophore at a low power (*e.g.*, 2
672 W/cm^2). For (d)STORM acquisitions, we began with AF647 or CellMask, followed by CF568. We
673 used an excitation power density of ~20 kW/cm^2 for shelving and blinking of CF568 and ~6-20
674 kW/cm^2 for AF647. The power density of the 405 nm illumination for both dyes was increased
675 from 0 to 50 W/cm^2 throughout an acquisition to keep the reactivation rate approximately
676 constant. The exposure time was 10.57 ms per frame and the calibrated EM gain was 43. The
677 image recording started after the initial shelving phase upon observation of clear SM blinking; the
678 blinking movies were acquired for approximately 60000 frames for each fluorophore.

679

680 *SR data analysis*

681 SM movies were processed with the ThunderStorm plugin[55] for Fiji. First, the images were filtered
682 with a wavelet filter with a b-spline order of 3 and a scale of 2. The coarse localizations were
683 found as local maxima with an 8-neighborhood connectivity and a threshold of 2·std(Wave.F1).
684 These localizations were weighted least squares-fitted with the integrated Gaussian model using

685 a radius of 4 pixels and an initial sigma of 1.1. Then, we performed drift correction estimated by
686 cross-correlation between successive subsets of localizations. For further processing, we kept
687 only localizations with fitted sigma between 160 nm and 80 nm.

688 For image registration, we imaged 200 nm TetraSpeck beads (T7280, Thermo Fisher Scientific) in
689 both channels, whose images were processed similarly to the SM movies. The transformation
690 between the channels was calculated using an affine transformation with help of Matlab function
691 'fitgeotrans'. The calculated transformation was then applied to the CF568 localizations using a
692 Matlab function 'transformPointsInverse'.

693 Localizations found within 50 nm on consecutive frames that could originate from multiple
694 localizations of a single molecule were treated in two ways. For SR images, these localizations
695 were refined to suppress overcounting by selecting them from a normal distribution with a mean
696 at the weighted mean of the initial localizations and a standard deviation (SD) that equals
697 $120 \cdot (N_{ph})^{-1/2}$ nm, where N_{ph} is the total number of photons acquired from all localizations in the
698 given consecutive series[38]. For data analysis other than SR image reconstruction, the localizations
699 of the consecutive series were reduced to a single localization at the weighted mean position.
700 The weights of localizations were proportional to the photon counts of these individual
701 localizations. SR images were reconstructed as 2D histograms with a bin size of 20 x 20 nm^2.
702 However, SR images where one of the channels contained the CellMask labelling had a bin size of
703 30 x 30 nm^2. SR images acquired with CellMask were additionally filtered with a Gaussian filter
704 with $\sigma = 0.5$ pixels.

705

706 *Cluster analysis with BIC-GMM*

707 Gaussian Mixture Models (GMM) implemented in Python were fitted to vgRNA and dsRNA
708 localization datasets, yielding a representation of localization densities as a collection of
709 potentially elliptical and/or rotated 2D Gaussians. The number of components most suitable for
710 each field of view was determined using an iterative grid search, evaluating 4 candidate GMMs
711 using the Bayesian Information Criterion (BIC)[56]. The first grid iteration tested [1, 2500]

712 components with test points t_i = { 1,834,1667,2500 } , where i denotes the index in the set such
713 that t_0 = 1. For each iteration of the grid search, the model with the lowest BIC was selected the
714 best candidate, t_k, and the next iteration of the grid was narrowed, to be bounded by [$t_{max\ (k-1,\ 0)}$
715 + 1, $t_{min\ (k+1,\ 3)}$ − 1], until the stride of the grid was 1 component, or the test point with the best BIC
716 was on a rail (k = 0 or 3). To reduce memory requirements, this GMM optimization was performed
717 on a random subset of up to 200,000 localizations from each data set, but the optimized GMM
718 was then used to predict a component assignment for all original localizations. These components
719 were regarded as clusters, and refined by removing localizations with a log probability of being
720 an event from their assigned Gaussian component of less than −25. The radius of gyration, *Rg*,
721 was then calculated for each cluster, and the number of localizations in each cluster, N_{loc}, was
722 used to approximate a cluster density as $\delta = N_{loc} / (\pi \cdot Rg^2)$. Clusters with δ below a threshold of
723 0.008 localizations/nm^2 for dsDNA, or below an ROI-dependent threshold between 0.005 and
724 0.013 localizations/nm^2 for vgRNA, were removed from further quantification as sparse
725 background. This analysis and resulting visualizations were carried out in the PYthon Microscopy
726 Environment (https://doi.org/10.5281/zenodo.4289803)[57], using a plugin
727 (github.com/barentine/bic-gmm) and the scikit-learn GMM implementation[58].

728

729 *Counting of vgRNA molecules in the clusters*

730 The number of vgRNA molecules in a vgRNA cluster was defined as a quotient between the
731 number of vgRNA-FISH localizations in the cluster and the average number of localizations
732 produced by a single FISH-labelled vgRNA molecule in the given cell. The average number of
733 localizations per vgRNA molecule was estimated from isolated nanoscale vgRNA puncta in the
734 cytoplasm (Supplementary Fig. 3a). This number was defined as the median of the number of
735 localizations within 50 nm from each localization in the region with vgRNA puncta. The estimated
736 number of vgRNA molecules was calculated for every cluster determined by the BIC-GMM cluster
737 analysis and the median value per cell was shown in a chart (Supplementary Fig. 3b-c).

738

739 *Counting of nsp12 puncta in the vgRNA clusters*

740 The center of nsp12 puncta is obtained by fitting the SR images in ThunderStorm[55]. The SR
741 localizations of nsp12 were first converted into a 2D histogram image with a bin size of 20 x 20
742 nm^2. The approximate localization of the center was found as a centroid of connected
743 components with a threshold of 5·std(Wave.F1) without filter. These localizations were least
744 squares-fitted with the integrated Gaussian model using a fitting radius of 2 pixels and an initial
745 sigma of 0.4. We next removed duplicates among localizations within a 20 nm radius. The puncta
746 whose sigma were smaller than 5 nm were further filtered out to avoid localizing single-pixel-
747 sized background localizations. For each vgRNA cluster with its center and the radius of gyration
748 (Rg) determined using BIC-GMM, we counted the number of nsp12 puncta within a 1.5·Rg
749 distance of the center of the vgRNA cluster. For nsp12 puncta found within the cutoff distance of
750 more than one vgRNA cluster, we assigned them to their closest cluster based on the relative
751 distance d/Rg, with d being the distance between the center of the vgRNA cluster and center of
752 the nsp12 punctum.

753

754 *Bivariate pair-correlation functions*

755 For calculation of bivariate pair-correlation functions[20] $g_{12}(r)$, we first manually selected the
756 cytoplasmic regions with dense vgRNA clusters. The pair-correlation functions were calculated by
757 counting the number of localizations of the second species within a distance between r and r+dr
758 from each localization of the first species. These were normalized by dividing the number of
759 localizations by the area of the corresponding ring of radii r and r+dr and by the average density
760 of the second species in the region. Finally, the obtained numbers were averaged across the
761 localizations of the first species. r was scanned over the range between 0 and 500 nm and dr was
762 set to 1 nm. For the complete spatial randomness (CSR) case, a test CSR dataset was generated
763 with the same average density as for the experimental case across the same ROI. $g_{12}(r)$ traces
764 were calculated from these CSR datasets as described above. No edge effect correction was
765 performed leading to a slight decrease of $g_{12}(r)$ at large r. Plots in the figures display experimental

766 and CSR $g_{12}(r)$ for each analyzed cell as faint lines as well as the mean $g_{12}(r)$ calculated from all
767 cells in bold lines.

768

769 *Estimation of RNA FISH labelling efficiency in virions*

770 Dye molecules inside virions were counted using fluorescence bleaching with SM calibration.
771 Virions attached to the coverslip were labelled using the RNA-FISH+IF protocol with PFA-only
772 fixation. The density of virions was around 0.5 μm^{-2} insuring observation of most virions as single
773 DL spots without overlap (Extended Data Fig. 1a, d). vgRNA was FISH-labelled with AF647 and
774 spike protein was IF-stained with CF568. Glass-bottom chambers with virions were kept in PBS for
775 this experiment. Samples were illuminated with 642 nm light at 20 W/cm^2 and were imaged with
776 an exposure time of 200 ms and an EM gain of 43 until bleaching of all AF647 in the imaging
777 region (around 200 s). A separate DL image of spike was taken with 560 nm excitation. The AF647
778 bleaching movies were processed in ThunderStorm using a wavelet filter with a b-spline order of
779 3 and a scale of 2, a local maximum approximate localization with a threshold of 1.2·std(Wave.F1)
780 and an 8-neighborhood connectivity. These localizations were weighted least squares-fitted with
781 the integrated Gaussian model using a radius of 3 pixels and an initial sigma of 1.1. Then, we kept
782 only localizations with sigma < 160 nm & sigma > 80 nm and removed duplicates within 300 nm
783 on each frame.

784 Further processing was done in Matlab with a custom script. We considered only vgRNA-AF647
785 localizations that had a spike-CF568 signal within 200 nm to avoid counting AF647 molecules
786 outside virions. The bleaching time traces (Extended Data Fig. 1c, f) were found by searching in
787 consecutive frames within 200 nm of the localization from the first frame and allowing up to 5
788 empty frames between frames with detections. The number of bleaching steps was defined as
789 the rounded quotient between the initial and the final brightness of a spot in a time trace serving
790 as the SM calibration. For each bleaching trace, the initial brightness (in photons) was defined as
791 the median value of the brightness in the first 4 localizations and the final brightness as the
792 median brightness value of the last 4 localizations. If the trace contained only 7-8 detections, the
793 range for the initial and the final brightness was reduced to 3 frames; for traces with 5-6

794 detections, this was reduced to 2; for traces with 3-4 frames – to 1; for traces containing only 1
795 or 2 detections, the number of bleaching steps was set to 1. For each analyzed region containing
796 around 200 bleaching traces, the number of bleaching steps was fitted with a zero-truncated
797 Poisson distribution (Extended Data Fig. 1g-h). The expected values ± SD obtained from the fit of
798 5 regions for each of not-treated and PK-treated cells are shown in a chart (Extended Data Fig.
799 1i).

800

801

802 **Author contribution**

803 L.A., M.H., L.S.Q. and W.E.M. conceived the project. L.A. designed the optical set-up, performed
804 the SR acquisitions and data analysis. M.H. performed cell culture, labelling and confocal imaging.
805 Y.Z. performed confocal and SR data analysis and helped with sample preparation and confocal
806 imaging. J.G. performed SARS-CoV-2 infection experiments at the BSL-3 facility with staff listed in
807 the Acknowledgements. A.R.R. contributed to the concept and SR experiments at the early stages
808 of the project. A.E.S.B. designed the BIC-GMM cluster analysis method and contributed to the
809 optical set-up design. L.A and W.E.M. wrote the manuscript with input from all authors.

810

811 **Acknowledgements**

812 We thank Puja Patel and Amol Pohane for their assistance with the cell culturing in the BSL3
813 facility. We thank Leiping Zeng for sample preparation and discussion about the results and
814 experimental plan with the other authors. This work was supported in part by the National
815 Institute of General Medical Sciences Grant Nos. R35GM118067 (to W.E.M.) and the National
816 Institutes of Health Common Fund 4D Nucleome Program No. U01 DK127405 (to L.S.Q.). We also
817 acknowledge Stanford University Cell Sciences Imaging Core Facility (RRID:SCR_017787). L.S.Q. is
818 a Chan Zuckerberg Biohub Investigator, and W.E.M. is a Sarafan ChEM-H Fellow.

819

References

1. Schmidt, N. *et al.* The SARS-CoV-2 RNA–protein interactome in infected human cells. *Nature Microbiology* **6**, 339-353 (2021).
2. Flynn, R.A. *et al.* Discovery and functional interrogation of SARS-CoV-2 RNA-host protein interactions. *Cell* **184**, 2394-2411.e2316 (2021).
3. Knoops, K. *et al.* SARS-coronavirus replication is supported by a reticulovesicular network of modified endoplasmic reticulum. *PLoS Biol* **6**, e226 (2008).
4. Snijder, E.J. *et al.* A unifying structural and functional model of the coronavirus replication organelle: Tracking down RNA synthesis. *PLoS Biol* **18**, e3000715 (2020).
5. Klein, S. *et al.* SARS-CoV-2 structure and replication characterized by in situ cryo-electron tomography. *Nat Commun* **11**, 5885 (2020).
6. Betzig, E. *et al.* Imaging intracellular fluorescent proteins at nanometer resolution. *Science* **313**, 1642-1645 (2006).
7. Rust, M.J., Bates, M. & Zhuang, X. Sub-diffraction-limit imaging by stochastic optical reconstruction microscopy (STORM). *Nat. Methods* **3**, 793-796 (2006).
8. Heilemann, M. *et al.* Subdiffraction-Resolution Fluorescence Imaging with Conventional Fluorescent Probes. *Angew. Chem. Int. Ed.* **47**, 6172-6176 (2008).
9. Klar, T.A., Jakobs, S., Dyba, M., Egner, A. & Hell, S.W. Fluorescence microscopy with diffraction resolution barrier broken by stimulated emission. *Proceedings of the National Academy of Sciences of the United States of America* **97**, 8206-8210 (2000).
10. Gustafsson, M.G.L. Surpassing the lateral resolution limit by a factor of two using structured illumination microscopy. *J. Microsc.* **198**, 82-87 (2000).
11. Xu, K., Zhong, G. & Zhuang, X. Actin, Spectrin, and Associated Proteins Form a Periodic Cytoskeletal Structure in Axons. *Science* **339**, 452-456 (2013).
12. Andronov, L., Ouararhni, K., Stoll, I., Klaholz, B.P. & Hamiche, A. CENP-A nucleosome clusters form rosette-like structures around HJURP during G1. *Nature Communications* **10**, 4436 (2019).
13. Reinhardt, S.C.M. *et al.* Ångström-resolution fluorescence microscopy. *Nature* **617**, 711-716 (2023).
14. Baddeley, D. & Bewersdorf, J. Biological Insight from Super-Resolution Microscopy: What We Can Learn from Localization-Based Images. *Annual Review of Biochemistry* **87**, 965-989 (2018).
15. Wang, J. *et al.* Multi-color super-resolution imaging to study human coronavirus RNA during cellular infection. *Cell Reports Methods* **2**, 100170 (2022).
16. Wolff, G. *et al.* A molecular pore spans the double membrane of the coronavirus replication organelle. *Science* **369**, 1395-1398 (2020).
17. Lee, J.Y. *et al.* Absolute quantitation of individual SARS-CoV-2 RNA molecules provides a new paradigm for infection dynamics and variant differences. *eLife* **11**, e74153 (2022).
18. Pepe, A., Pietropaoli, S., Vos, M., Barba-Spaeth, G. & Zurzolo, C. Tunneling nanotubes provide a route for SARS-CoV-2 spreading. *Science Advances* **8**, eabo0171 (2022).
19. Sherman, E. *et al.* Functional Nanoscale Organization of Signaling Molecules Downstream of the T Cell Antigen Receptor. *Immunity* **35**, 705-720 (2011).
20. Razvag, Y., Neve-Oz, Y., Sajman, J., Reches, M. & Sherman, E. Nanoscale kinetic segregation of TCR and CD45 in engaged microvilli facilitates early T cell activation. *Nature Communications* **9**, 732 (2018).

21. Sawicki, S.G. & Sawicki, D.L. Coronavirus minus-strand RNA synthesis and effect of cycloheximide on coronavirus RNA synthesis. *Journal of Virology* **57**, 328-334 (1986).
22. Hillen, H.S. *et al.* Structure of replicating SARS-CoV-2 polymerase. *Nature* **584**, 154-156 (2020).
23. Gao, Y. *et al.* Structure of the RNA-dependent RNA polymerase from COVID-19 virus. *Science* **368**, 779-782 (2020).
24. Ahn, D.-G., Choi, J.-K., Taylor, D.R. & Oh, J.-W. Biochemical characterization of a recombinant SARS coronavirus nsp12 RNA-dependent RNA polymerase capable of copying viral RNA templates. *Archives of Virology* **157**, 2095-2104 (2012).
25. Naydenova, K. *et al.* Structure of the SARS-CoV-2 RNA-dependent RNA polymerase in the presence of favipiravir-RTP. *Proceedings of the National Academy of Sciences* **118**, e2021946118 (2021).
26. Eymieux, S. *et al.* Ultrastructural modifications induced by SARS-CoV-2 in Vero cells: a kinetic analysis of viral factory formation, viral particle morphogenesis and virion release. *Cellular and Molecular Life Sciences* **78**, 3565-3576 (2021).
27. Cortese, M. *et al.* Integrative Imaging Reveals SARS-CoV-2-Induced Reshaping of Subcellular Morphologies. *Cell Host & Microbe* **28**, 853-866.e855 (2020).
28. Lang, S. *et al.* An Update on Sec61 Channel Functions, Mechanisms, and Related Diseases. *Front Physiol* **8**, 887 (2017).
29. Hsu, J.C.-C., Laurent-Rolle, M., Pawlak, J.B., Wilen, C.B. & Cresswell, P. Translational shutdown and evasion of the innate immune response by SARS-CoV-2 NSP14 protein. *Proceedings of the National Academy of Sciences* **118**, e2101161118 (2021).
30. Mönkemöller, V. *et al.* Imaging fenestrations in liver sinusoidal endothelial cells by optical localization microscopy. *Physical Chemistry Chemical Physics* **16**, 12576-12581 (2014).
31. Oudshoorn, D. *et al.* Expression and Cleavage of Middle East Respiratory Syndrome Coronavirus nsp3-4 Polyprotein Induce the Formation of Double-Membrane Vesicles That Mimic Those Associated with Coronaviral RNA Replication. *mBio* **8**, 10.1128/mbio.01658-01617 (2017).
32. Liv, Z. *et al.* SARS-CoV-2 nsp3-4 suffice to form a pore shaping replication organelles. *bioRxiv*, 2022.2010.2021.513196 (2022).
33. Han, Y.-S. *et al.* Papain-Like Protease 2 (PLP2) from Severe Acute Respiratory Syndrome Coronavirus (SARS-CoV): Expression, Purification, Characterization, and Inhibition. *Biochemistry* **44**, 10349-10359 (2005).
34. Shin, D. *et al.* Papain-like protease regulates SARS-CoV-2 viral spread and innate immunity. *Nature* **587**, 657-662 (2020).
35. Hartenian, E. *et al.* The molecular virology of coronaviruses. *J Biol Chem* **295**, 12910-12934 (2020).
36. V'Kovski, P., Kratzel, A., Steiner, S., Stalder, H. & Thiel, V. Coronavirus biology and replication: implications for SARS-CoV-2. *Nat Rev Microbiol* **19**, 155-170 (2021).
37. Baggen, J., Vanstreels, E., Jansen, S. & Daelemans, D. Cellular host factors for SARS-CoV-2 infection. *Nature Microbiology* **6**, 1219-1232 (2021).
38. Andronov, L., Genthial, R., Hentsch, D. & Klaholz, B.P. splitSMLM, a spectral demixing method for high-precision multi-color localization microscopy applied to nuclear pore complexes. *Communications Biology* **5**, 1100 (2022).
39. Storti, B. *et al.* A spatial multi-scale fluorescence microscopy toolbox discloses entry checkpoints of SARS-CoV-2 variants in Vero E6 cells. *Computational and Structural Biotechnology Journal* **19**, 6140-6156 (2021).
40. Scherer, K.M. *et al.* SARS-CoV-2 nucleocapsid protein adheres to replication organelles before viral assembly at the Golgi/ERGIC and lysosome-mediated egress. *Science Advances* **8**, eabl4895 (2022).
41. Cao, C. *et al.* The architecture of the SARS-CoV-2 RNA genome inside virion. *Nature Communications* **12**, 3917 (2021).

42. Lan, T.C.T. *et al.* Secondary structural ensembles of the SARS-CoV-2 RNA genome in infected cells. *Nature Communications* **13**, 1128 (2022).
43. Gopal, A., Zhou, Z.H., Knobler, C.M. & Gelbart, W.M. Visualizing large RNA molecules in solution. *RNA* **18**, 284-299 (2012).
44. Schonborn, J. *et al.* Monoclonal antibodies to double-stranded RNA as probes of RNA structure in crude nucleic acid extracts. *Nucleic Acids Res* **19**, 2993-3000 (1991).
45. Ku, J. *et al.* Reactive Polymer Targeting dsRNA as Universal Virus Detection Platform with Enhanced Sensitivity. *Biomacromolecules* **21**, 2440-2454 (2020).
46. Deng, J. *et al.* SARS-CoV-2 NSP8 suppresses type I and III IFN responses by modulating the RIG-I/MDA5, TRIF, and STING signaling pathways. *Journal of Medical Virology* **95**, e28680 (2023).
47. Kumar, P. *et al.* The nonstructural protein 8 (nsp8) of the SARS coronavirus interacts with its ORF6 accessory protein. *Virology* **366**, 293-303 (2007).
48. Snijder, E.J. *et al.* Ultrastructure and origin of membrane vesicles associated with the severe acute respiratory syndrome coronavirus replication complex. *J Virol* **80**, 5927-5940 (2006).
49. Stertz, S. *et al.* The intracellular sites of early replication and budding of SARS-coronavirus. *Virology* **361**, 304-315 (2007).
50. Ulasli, M., Verheije, M.H., de Haan, C.A.M. & Reggiori, F. Qualitative and quantitative ultrastructural analysis of the membrane rearrangements induced by coronavirus. *Cellular Microbiology* **12**, 844-861 (2010).
51. Chiem, K., Ye, C. & Martinez-Sobrido, L. Generation of Recombinant SARS-CoV-2 Using a Bacterial Artificial Chromosome. *Current Protocols in Microbiology* **59**, e126 (2020).
52. Ye, C. *et al.* Rescue of SARS-CoV-2 from a Single Bacterial Artificial Chromosome. *mBio* **11**, 10.1128/mbio.02168-02120 (2020).
53. Schindelin, J. *et al.* Fiji: an open-source platform for biological-image analysis. *Nature methods* **9**, 676-682 (2012).
54. Barentine, A.E.S. *et al.* An integrated platform for high-throughput nanoscopy. *Nature Biotechnology* (2023).
55. Ovesny, M., Krizek, P., Borkovec, J., Svindrych, Z. & Hagen, G.M. ThunderSTORM: a comprehensive ImageJ plug-in for PALM and STORM data analysis and super-resolution imaging. *Bioinformatics (Oxford, England)* **30**, 2389-2390 (2014).
56. Schwarz, G. Estimating the dimension of a model. *The annals of statistics* **6**, 461-464 (1978).
57. Marin, Z. *et al.* PYMEVisualize: an open-source tool for exploring 3D super-resolution data. *Nature Methods* **18**, 582-584 (2021).
58. Pedregosa, F. *et al.* Scikit-learn: Machine Learning in Python. *J. Mach. Learn. Res.* **12**, 2825–2830 (2011).

Extended Data Figures

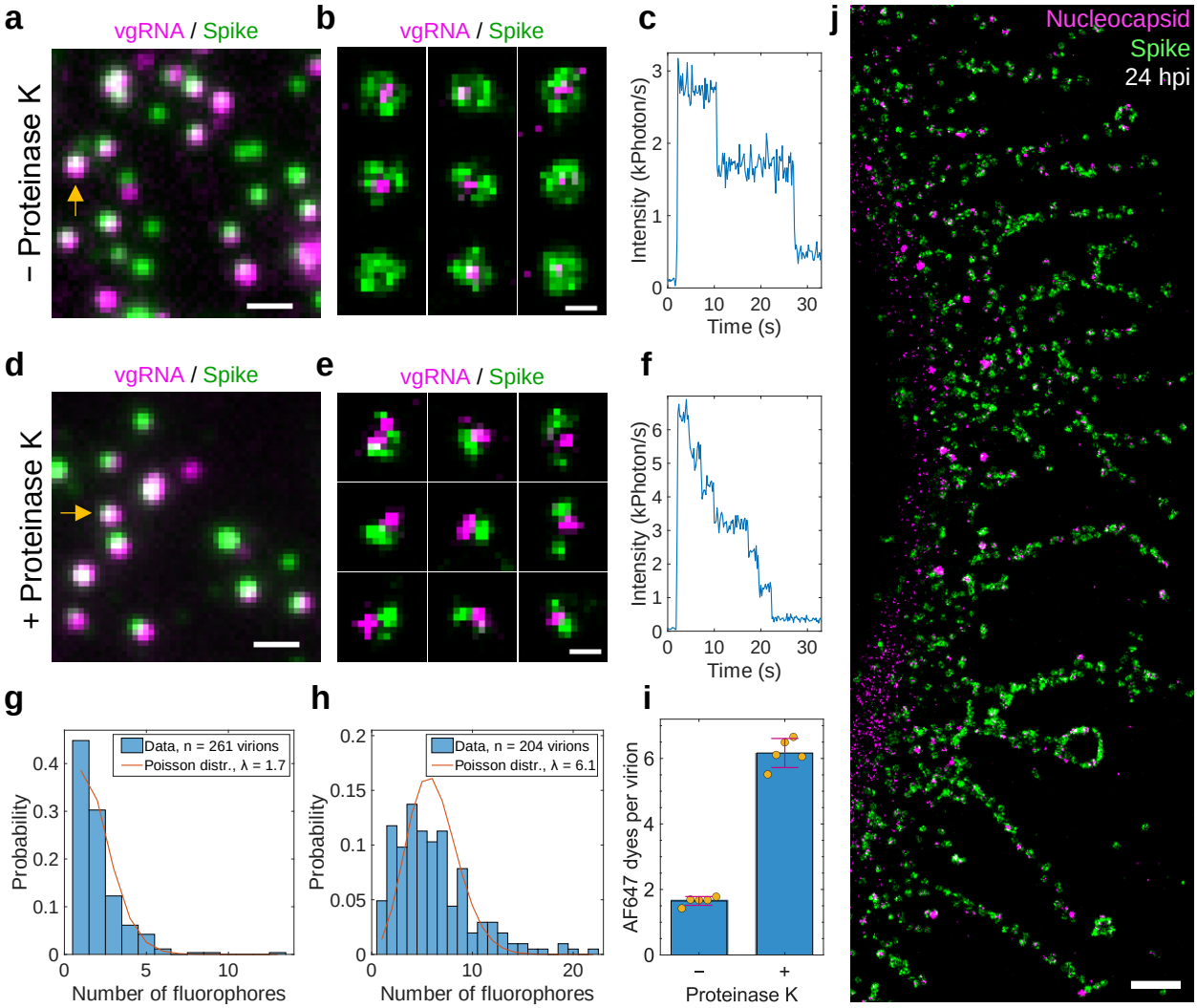

Extended Data Fig. 1. Validation of the labelling and imaging approach.

a, DL image of SARS-CoV-2 virions where vgRNA was labelled with AF647 by RNA FISH and the spike proteins were labelled by primary anti-spike S2 antibody with secondary CF568-conjugated antibody. **b**, Representative two-color SR images of individual virions reveal concentric localization of spike around vgRNA. **c**, Bleaching time trace of AF647 emission from a single virion (yellow arrow in **a**) demonstrates two-step bleaching. **d**, DL image of virions that were treated with Proteinase K (PK) before labelling. **e**, SR images of PK-treated virions reveal incomplete spike labelling due to digestion of proteins by the PK. **f**, Bleaching time trace of AF647 emission from a single virion (yellow arrow in **d**) shows 6-step bleaching suggesting increased vgRNA labelling efficiency in PK-treated virions. **g**-**h**, Histograms of the number of fluorophores per virion in

964 untreated (**g**) or PK-treated (**h**) samples and their fits with a Poisson distribution. **i**, Mean number
965 of AF647 molecules per virion from the fit for 5 different regions in both untreated and PK-treated
966 samples. p-value = $2 \cdot 10^{-8}$, two-tailed t-test. The error bar indicates mean ± SD value for the
967 untreated and PK-treated groups. **j**, SR image of a SARS-CoV-2 infected cell with the cell body to
968 the left reveals assembled virions at its cytoplasmic tubular projections at 24 hpi. Scale bars, 100
969 nm (**b**, **e**) and 1 µm (**a**, **d**, **j**).

970

971

972

973

974

975

976

977

978

979

980

981

982

983

984

985

986

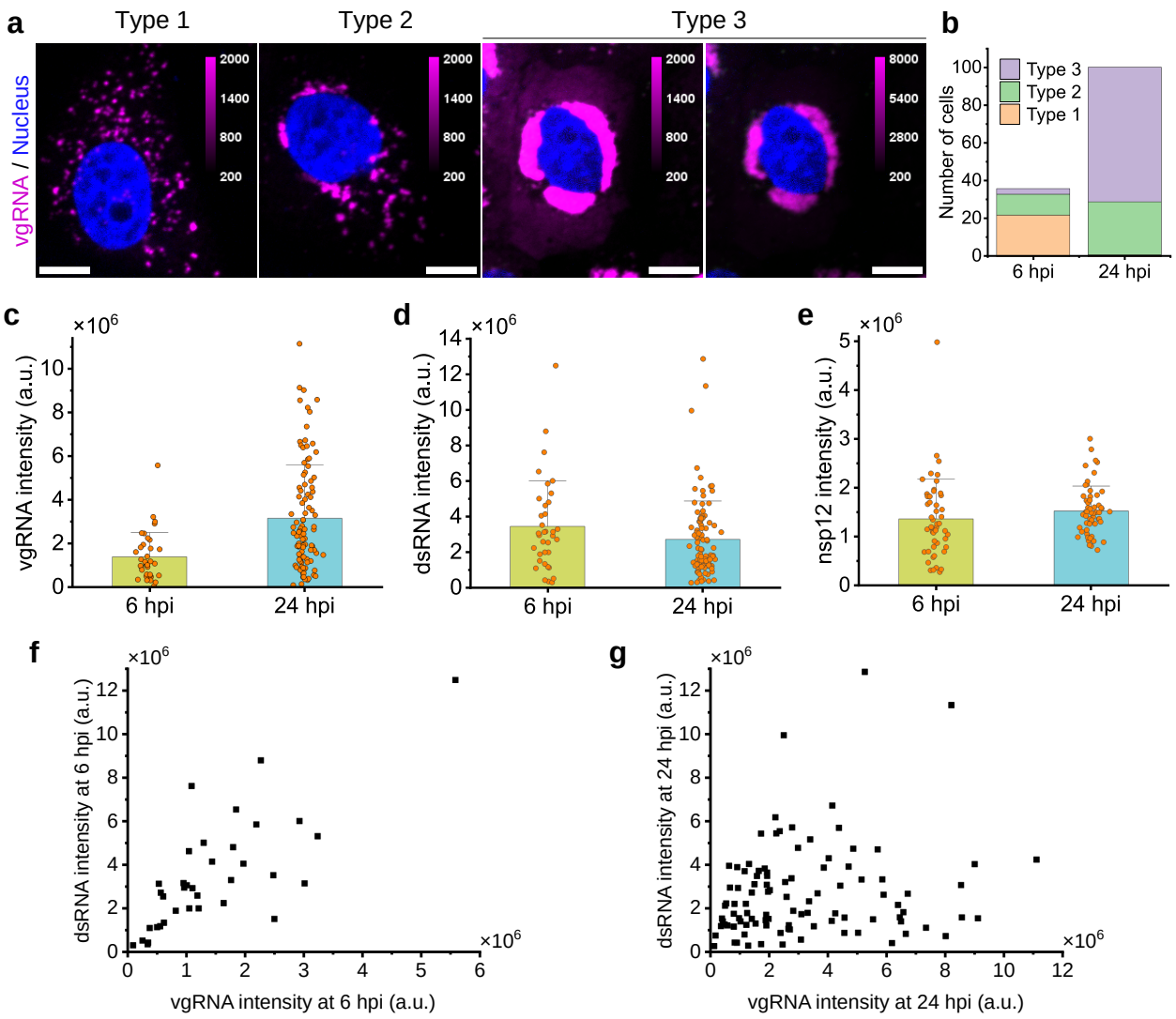

Extended Data Fig. 2. Screening and quantification of vgRNA, dsRNA and nsp12 by confocal microscopy.

a, Representative confocal images show three types of vgRNA distribution in SARS-CoV-2 infected cells. **b**, Number of cells assigned to one of the three types at 6 or 24 hpi. **c**, Cell-integrated vgRNA signal increases significantly from 6 hpi to 24 hpi. p-value = $6 \cdot 10^{-8}$, two-tailed t-test. **d**-**e**, Cell-integrated signal of immunofluorescently detected dsRNA (**d**) and nsp12 (**e**) in SARS-CoV-2 infected cells does not significantly change from 6 hpi to 24 hpi. p-values = 0.13 (**d**) and 0.23 (**e**), two-tailed t-test. **f**, dsRNA signal correlates with vgRNA signal at 6 hpi (Pearson's r = 0.76). **g**, dsRNA signal does not correlate with vgRNA signal at 24 hpi (Pearson's r = 0.18). Error bars represent mean + SD of the values from individual cells. Scale bars, 10 µm.

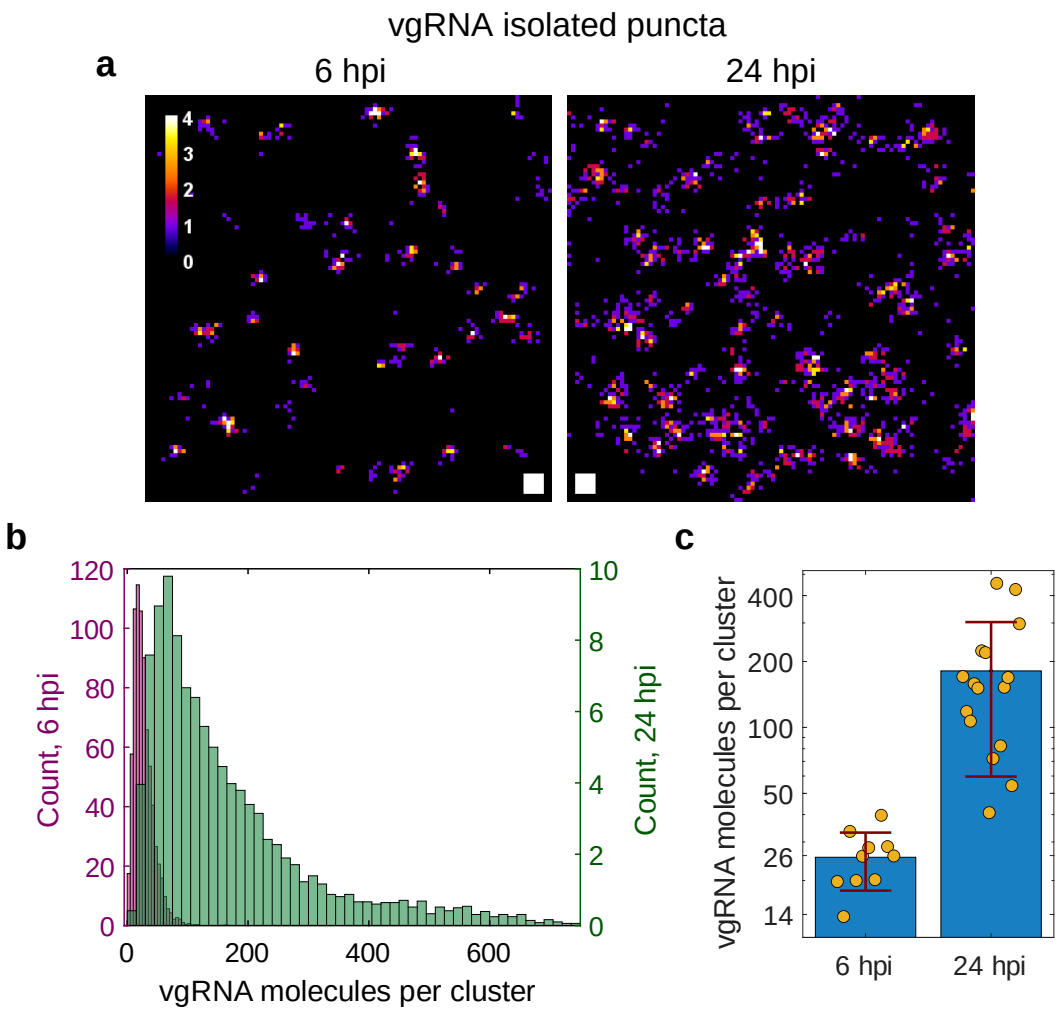

Extended Data Fig. 3. Estimation of the number of vgRNA molecules in vgRNA clusters.

a, SR localizations of single vgRNA molecules found in the cytoplasm of infected cells outside the dense vgRNA clusters. On a cell by cell basis, similar images are used as a calibration for the number of SR detections per one vgRNA molecule. **b**, The estimated number of vgRNA molecules per cluster at 6 and 24 hpi from all analyzed cells. The histogram counts are normalized by the number of analyzed cells; the histogram counts for 24 hpi are additionally divided by 3 to account for the 3x wider bin size than at 6 hpi. **c**, Median estimated counts of vgRNA molecules per cluster for each analyzed cell (individual yellow points). The error bars represent mean ± SD values of these median vgRNA molecule counts for each time point. p-value = $5 \cdot 10^{-4}$, two-tailed t-test. Scale bars, 50 nm x 50 nm.

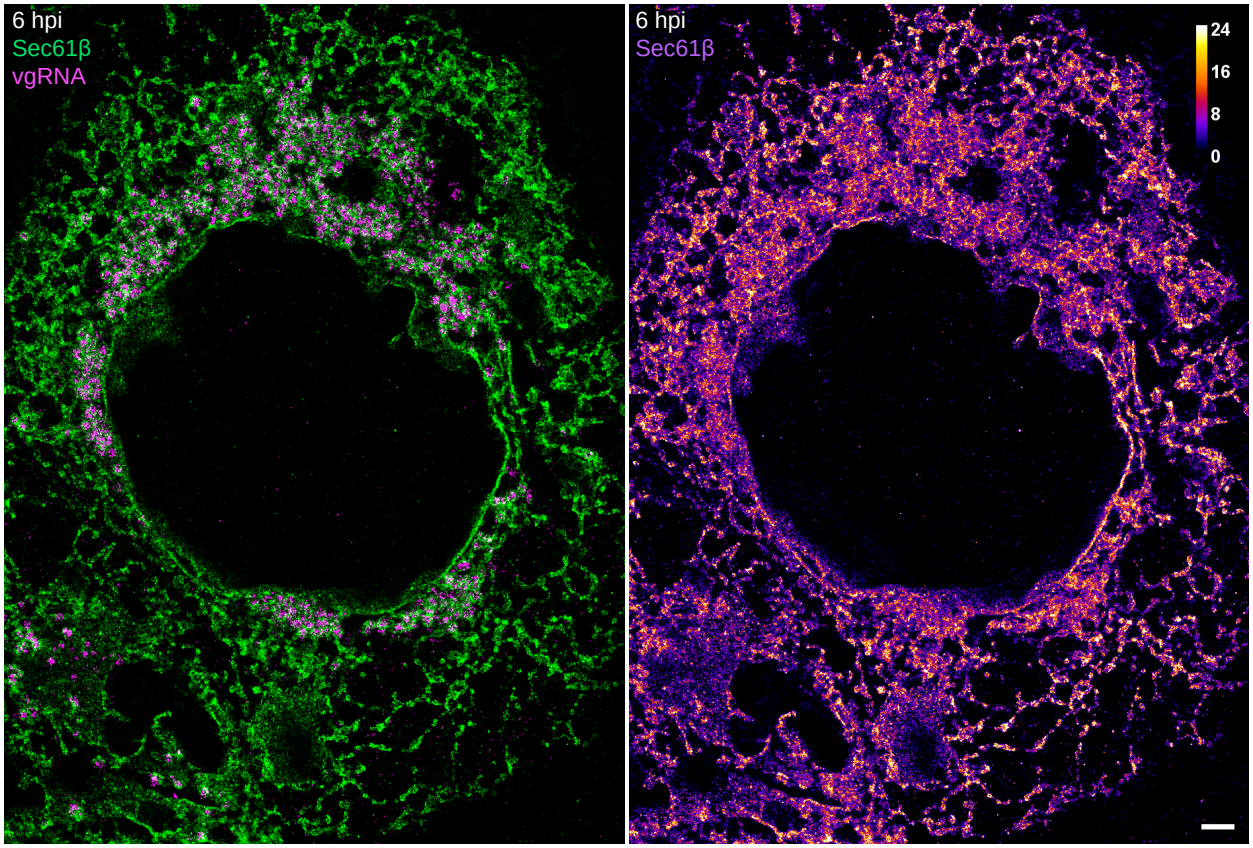

Extended Data Fig. 4. Host ER modification at 6 hpi.

SR image of vgRNA in a SARS-CoV-2 infected Vero E6 cell, stably expressing Sec61β-GFP. Altered ER forms ring-like structures that partially encapsulate vgRNA clusters in the perinuclear region. Left: green/magenta coloring; right: color scale of localizations. Scale bar, 1 µm.

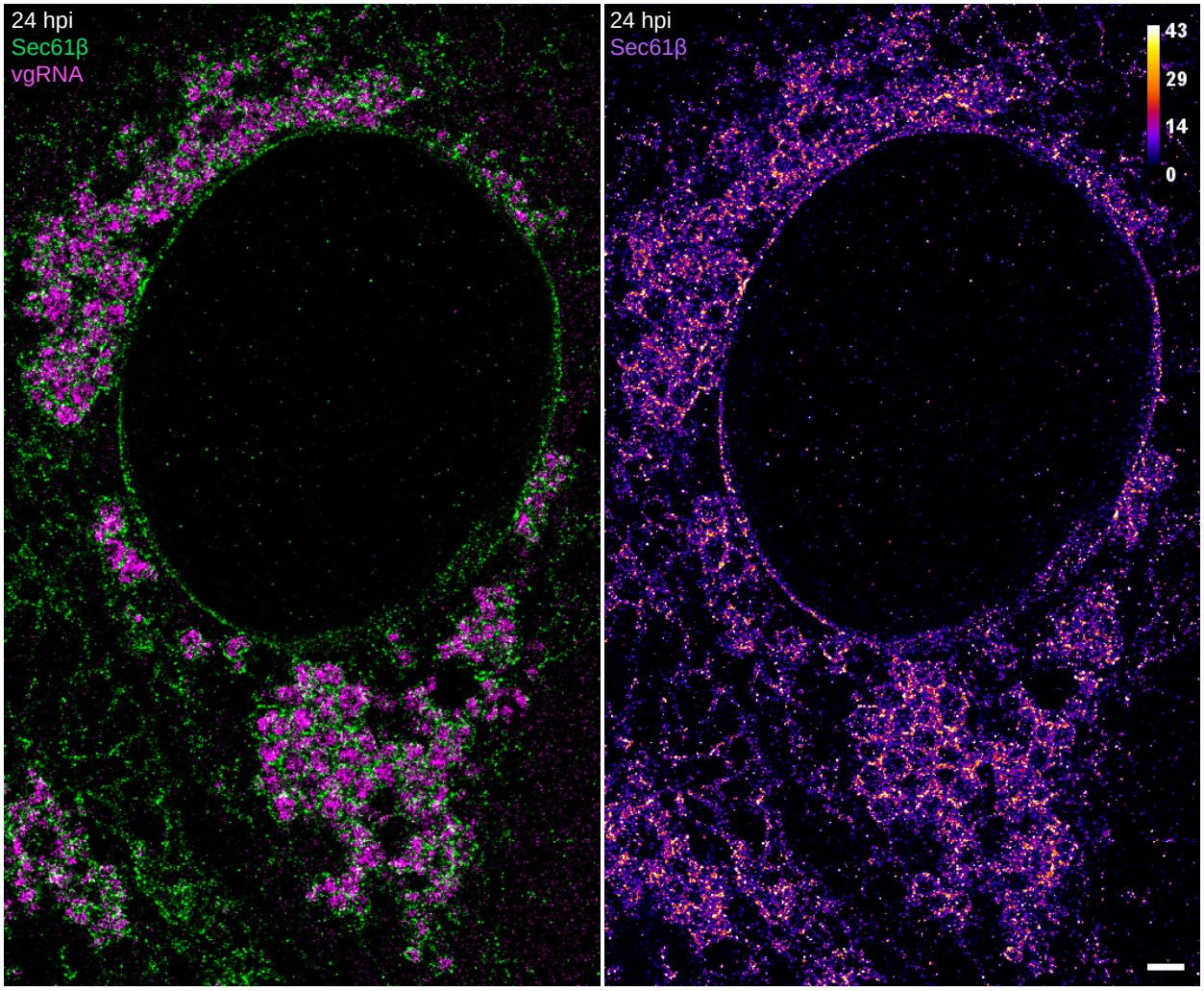

Extended Data Fig. 5. Host ER modification at 24 hpi.

SR image of vgRNA in a SARS-CoV-2 infected Vero E6 cell, stably expressing Sec61β-GFP. Altered ER forms ring-like structures that encapsulate vgRNA clusters in the perinuclear region, while the Sec61β signal at the ER tubules decreases compared to 6 hpi (Extended Data Fig. 4). Scale bar, 1 µm.

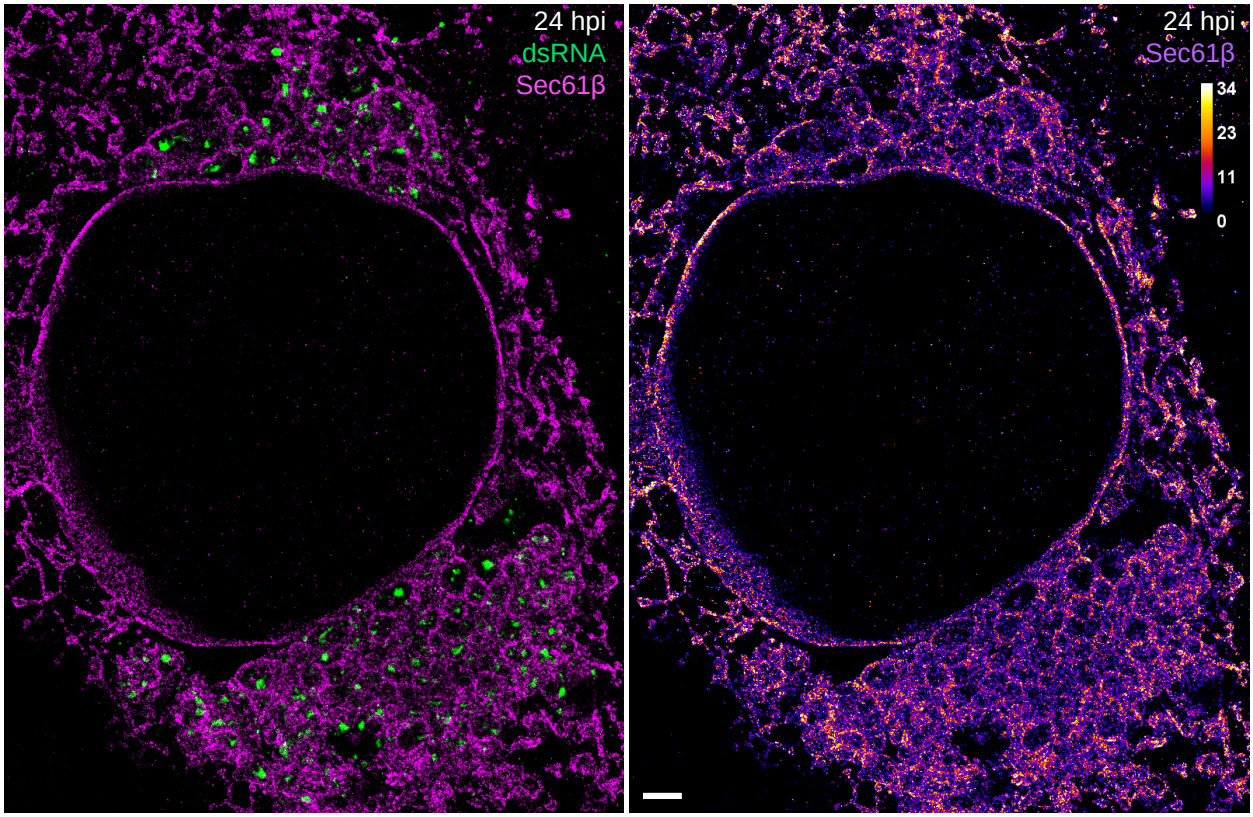

Extended Data Fig. 6. Encapsulation of dsRNA by altered host ER at 24 hpi.

SR image of dsRNA in a SARS-CoV-2 infected Vero E6 cell, stably expressing Sec61β-GFP. Ring-like structures of altered ER encapsulate dsRNA clusters. Scale bar, 1 µm.

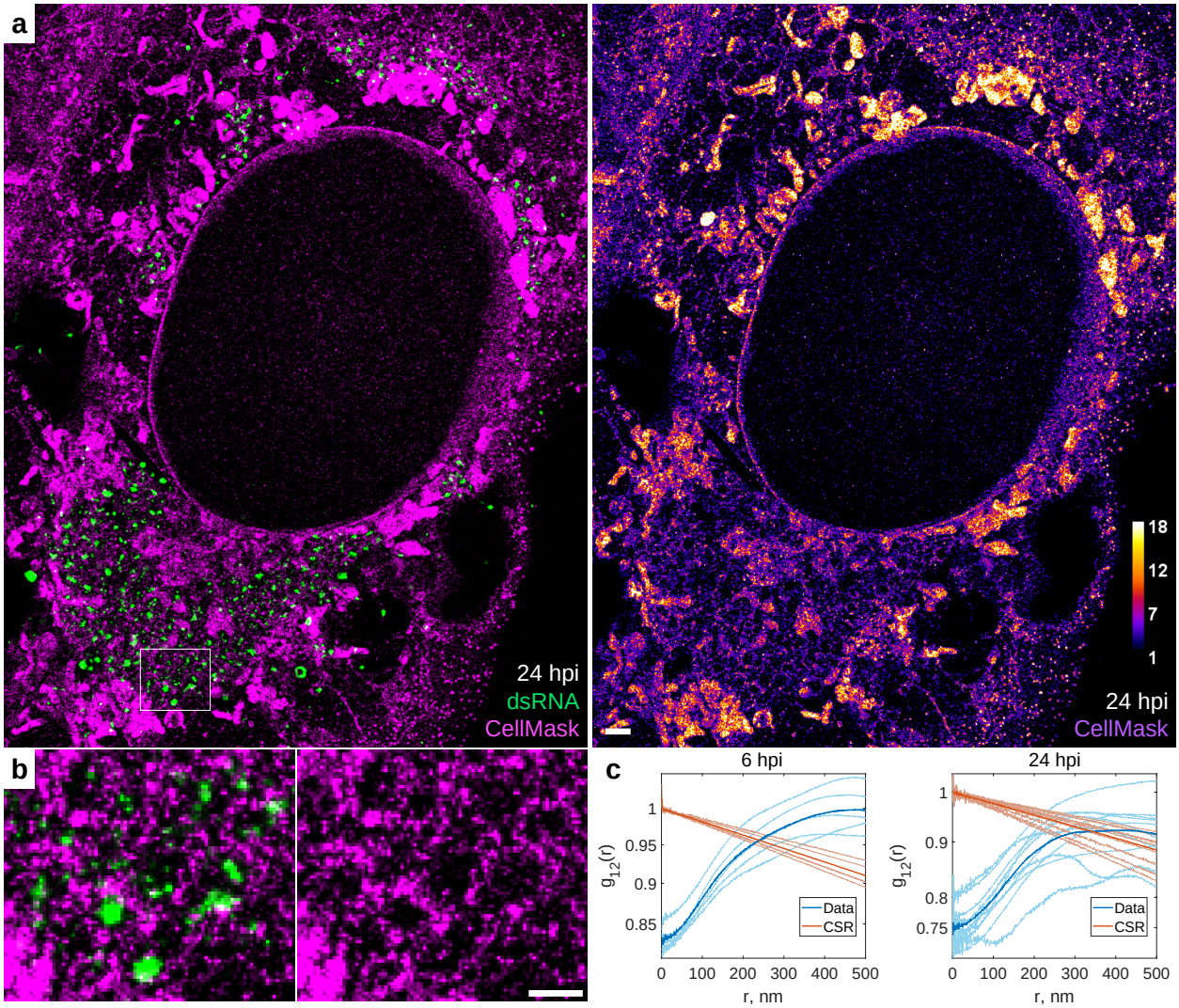

Extended Data Fig. 7. dsRNA is encapsulated into membrane-bound organelles.

a, SR image of dsRNA in a SARS-CoV-2 infected cell at 24 hpi with membranes labelled by CellMask Deep Red and dsRNA labelled with immunofluorescence. CellMask-labelled membranes can be observed around dsRNA clusters. Virions at the plasma membrane are seen as bright puncta (right side and lower right corner of the image). **b**, Zoomed-in image that corresponds to the white box in **a**. **c**, Bivariate pair-correlation functions indicate nanoscale anti-correlation between dsRNA and CellMask, consistent with dsRNA encapsulation in membrane-bound organelles at both 6 and 24 hpi. Scale bar, 1 µm (**a**) and 500 nm (**b**).

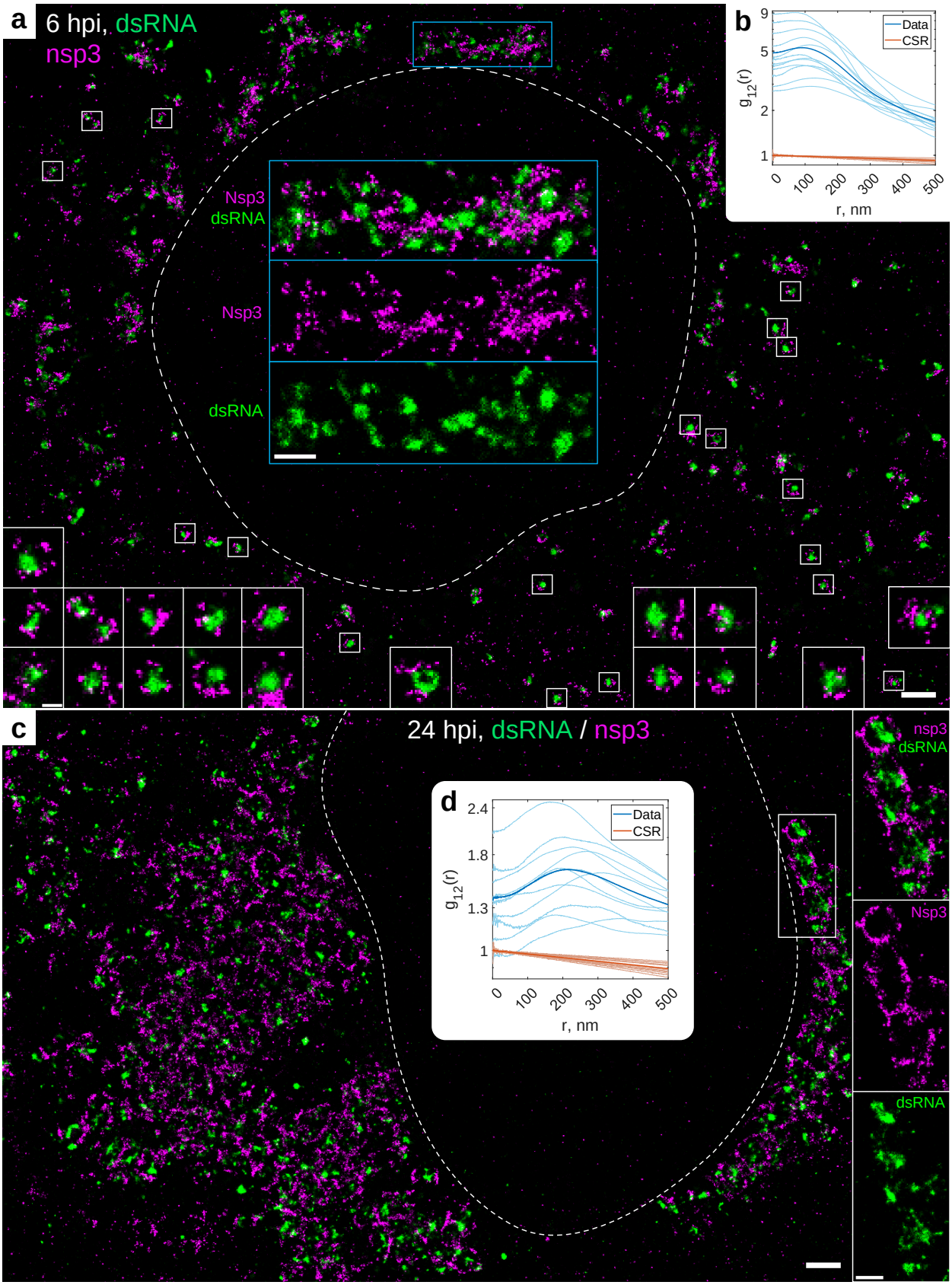
a
6 hpi, dsRNA
nsp3
Nsp3
dsRNA
Nsp3
dsRNA
b
Data
CSR
$g_{12}(r)$
r, nm
c
24 hpi, dsRNA / nsp3
d
Data
CSR
$g_{12}(r)$
r, nm
nsp3
dsRNA
Nsp3
dsRNA

1058

1059 **Extended Data Fig. 8. Nsp3 anti-correlates with dsRNA.**

1060 **a**, SR image of a SARS-CoV-2 infected cell at 6 hpi with nsp3 and dsRNA labelled by
1061 immunofluorescence. Nsp3 can be observed at the surface of isolated dsRNA clusters (white
1062 boxes & white insets) or in dense aggregates between dsRNA clusters (blue boxes & blue insets).
1063 **b**, Bivariate pair-correlation functions indicate nanoscale anti-correlation between dsRNA and
1064 nsp3 at 6 hpi. **c**, SR image of a SARS-CoV-2 infected cell at 24 hpi with nsp3 and dsRNA labelled by
1065 immunofluorescence. Nsp3 forms a network-like pattern that encapsulates dsRNA clusters. **d**,
1066 Bivariate pair-correlation functions indicate nanoscale anti-correlation between dsRNA and nsp3
1067 at 24 hpi. Scale bars, 1 µm (**a**, **c**), 500 nm (blue insets in **a** and insets in **c**) and 200 nm (white insets
1068 in **a**).

1069

1070

1071

1072

1073

1074

1075

1076

1077

1078

1079

1080

1081

1082

1083

1084

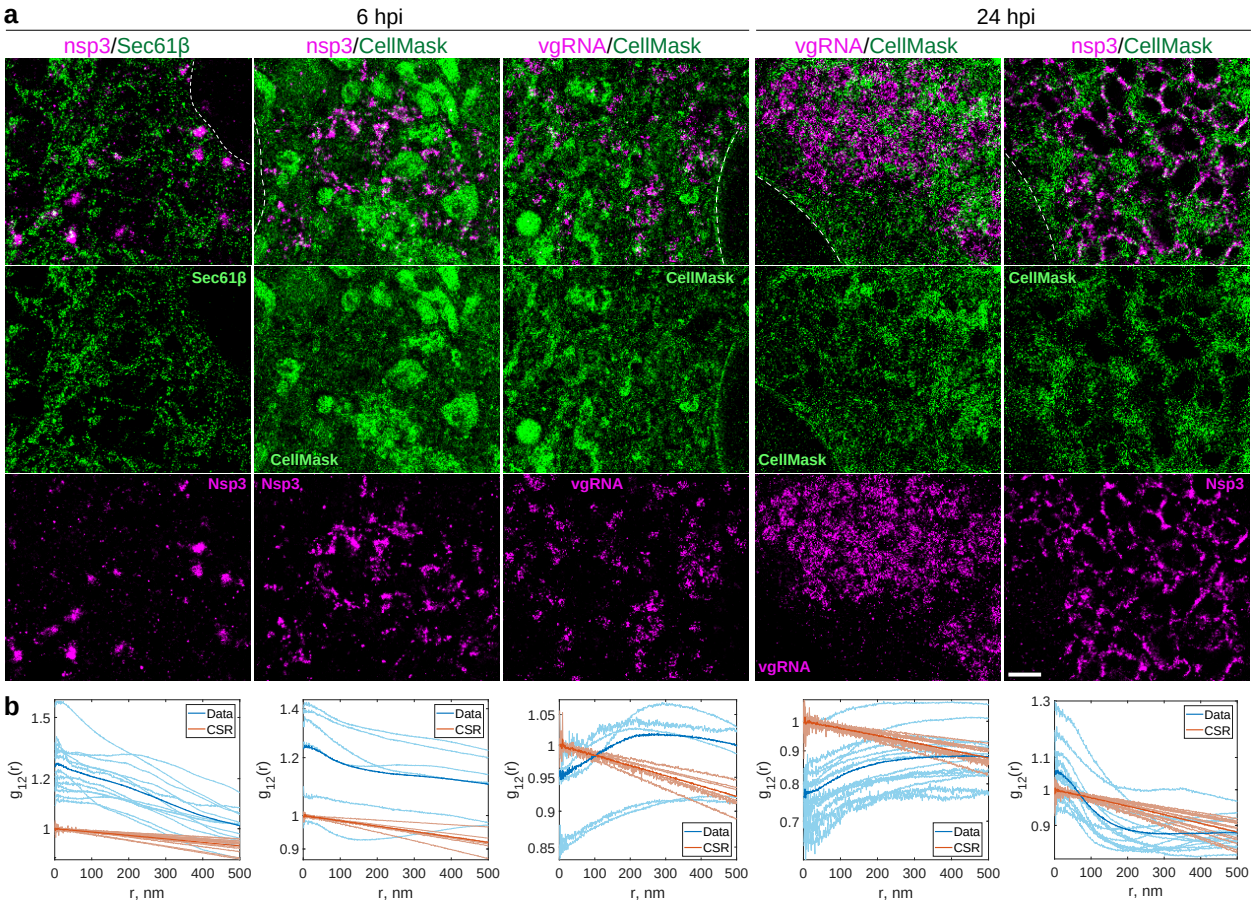

Extended Data Fig. 9. Nanoscale co-organization of viral components with host membranes.

a, SR images of nsp3, Sec61β, vgRNA and membranes (CellMask) in SARS-CoV-2 infected cells at 6 and 24 hpi. **b**, Bivariate pair-correlation functions indicate nanoscale association between nsp3 and Sec61β, nsp3 and CellMask and nanoscale anti-correlation between vgRNA and CellMask at both time points. Scale bar, 1 µm.

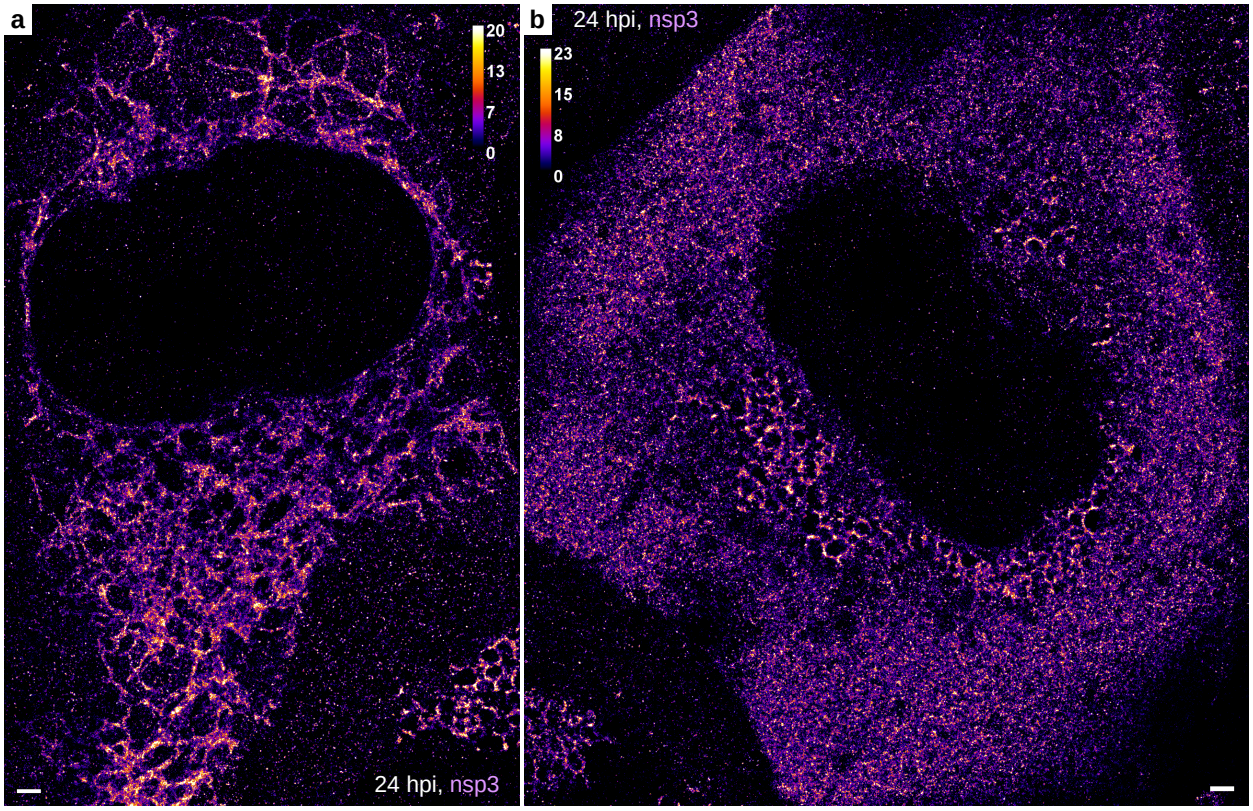

Extended Data Fig. 10. Less common patterns of nanoscale nsp3 localization at 24 hpi.

a, Nsp3 forms an ER-like network that occupies a large part of the cytoplasm. **b**, Besides the common perinuclear pattern, Nsp3 is also diffusely localized throughout the whole cytoplasm. Scale bars, 1 µm.